



HAL
open science

Engineering open-shell extended edge states in chiral graphene nanoribbons on MgO

Amelia Domínguez-Celorrio, Leonard Edens, Sofía Sanz, Manuel Vilas-Varela, Jose Martinez-Castro, Diego Peña, Véronique Langlais, Thomas Frederiksen, José I Pascual, David Serrate

► **To cite this version:**

Amelia Domínguez-Celorrio, Leonard Edens, Sofía Sanz, Manuel Vilas-Varela, Jose Martinez-Castro, et al.. Engineering open-shell extended edge states in chiral graphene nanoribbons on MgO. 2024. hal-04784863

HAL Id: hal-04784863

<https://hal.science/hal-04784863v1>

Preprint submitted on 15 Nov 2024

HAL is a multi-disciplinary open access archive for the deposit and dissemination of scientific research documents, whether they are published or not. The documents may come from teaching and research institutions in France or abroad, or from public or private research centers.

L'archive ouverte pluridisciplinaire **HAL**, est destinée au dépôt et à la diffusion de documents scientifiques de niveau recherche, publiés ou non, émanant des établissements d'enseignement et de recherche français ou étrangers, des laboratoires publics ou privés.

Engineering open-shell extended edge states in chiral graphene nanoribbons on MgO

Amelia Domínguez-Celorrio^{1,2,3,†}, Leonard Edens^{4, †}, Sofía Sanz⁵, Manuel Vilas-Varela⁶, Jose Martinez-Castro⁷, Diego Peña⁶, Véronique Langlais⁸, Thomas Frederiksen^{5,9}, José I. Pascual^{4,9}, and David Serrate^{1,10,11*}

¹Instituto de Nanociencia y Materiales de Aragón (INMA), CSIC-Universidad de Zaragoza, Zaragoza, E-50009, Spain

²School of Physics and Astronomy, Monash University, Clayton, VIC 3800, Australia

³ARC Centre for Future Low Energy Electronics Technologies, Monash University, Clayton, VIC 3800, Australia

⁴CIC NanoGUNE BRTA, San Sebastián, E-20018, Spain

⁵Donostia International Physics Center, San Sebastián, E-20018, Spain.

⁶Centro Singular de Investigación en Química Bilóxica e Materiais Moleculares (CiQUS) and Departamento de Química Orgánica, Universidade de Santiago de Compostela, Santiago de Compostela, E-15782, Spain.

⁷Peter Grünberg Institut (PGI-3), Forschungszentrum Jülich, 52425 Jülich, Germany

⁸Centre d'Elaboration de Materiaux et d'Etudes Structurales, CNRS, Toulouse, F-31055 France

⁹Ikerbasque, Basque Foundation for Science, Bilbao, E-48013, Spain.

¹⁰Departamento de Física de la Materia Condensada, Universidad de Zaragoza, Zaragoza, E-50009, Spain

¹¹Laboratorio de Microscopias Avanzadas (LMA), Universidad de Zaragoza, Zaragoza, E-50018, Spain.

†These authors contributed equally

*email: serrate@unizar.es

Graphene nanostructures are a promising platform for engineering electronic states with tailored magnetic and quantum properties. Synthesis strategies on metallic substrates have made it possible to manufacture atomically precise nanographenes with controlled size, shape and edge geometry. In these nanographenes, finite spin magnetic moment can arise as a result of many-body interactions in molecular orbitals with π -conjugated character and subject to strong spatial confinement, for example at the zig-zag edges. However, owing to the mixing of the molecular orbitals and metallic states from the catalysing substrate, most of their expected quantum phenomenology is severely hindered. The use of in-situ ultra-thin decoupling layers can impede nanographene-metal hybridization and facilitate the expression of predicted properties. Here we show that the edges of narrow chiral graphene nanoribbons (GNRs) over MgO monolayers on Ag(001) can host integer charge and spin-1/2 frontier states. The electron occupation varies with the GNR length, which alternates even or odd number of electrons, thus resulting correspondingly in a non-magnetic closed-shell state or an open-shell paramagnetic system. For the latter, we found the spectral fingerprint of a narrow Coulomb correlation gap. Charged states, up to 19 additional electrons, were identified by comparing mean-field Hubbard (MFH) simulations of the density of states with experimental maps of the discretized molecular orbitals acquired with a scanning tunnelling microscope (STM). In consideration of the length-dependent magnetic moment and the discrete nature of the electronic structure, we envisage that GNRs supported by thin insulating films can be used as tailor-made active elements in quantum sensing and quantum information processing.

INTRODUCTION

When graphene is shaped with atomic precision into certain customized geometries, its conjugated π -electron lattice can exhibit a wealth of novel phenomenology resulting from the extended electronic interactions and correlations. For example, the band structure of graphene nanoribbons (GNRs) can be tuned with their size, orientation, and composition [1–7]. This enables full control of their functionality, ranging from semiconducting to metallic [4,8–10], or exhibiting zero-energy states such as edge-localized bands [11,12] and symmetry-protected topological boundary states [8,9,13]. The confirmation of these predictions was achieved with the emergence of on-surface synthesis (OSS) as a reliable strategy for the bottom-up fabrication of customized graphene nanostructures, offering meticulous control over shape, size, and edge topology [14,15]. Specifically, OSS involves steered reactions of organic precursors designed to form specific molecular structures under the catalytic action of a metallic surface [14–16]. Low-temperature scanning tunnelling spectroscopy (STS) has corroborated the targeted band structure of various GNRs, as well as the existence of zero-energy states, together with the concomitant emergence of paramagnetism [17–19] and non-local magnetic order [20].

In the conventional OSS approach, the intrinsic electronic states of GNRs and other nanographenes hybridize with the metallic support, which is detrimental to most of their potential applications. In particular, it gives rise to the appearance of multiple relaxation channels for electron and spin quantum states, broadening the theoretically discrete energy spectrum, and substantially shortening the electron-spin coherence times (compared to the intrinsic ones estimated to be $\gtrsim 200 \mu\text{s}$ [21,22]). The 1D nature of the GNR edge states causes an additional adverse effect of the hybridization: since they have a large spatial extent, the electronic correlations –responsible for the emergence of spin moments–become vanishingly irrelevant for increasing length (increasing delocalization). In order to preserve the quantum behaviour of electronic and magnetic degrees of freedom in nanographenes, it is necessary to progress towards their electronic decoupling from the catalysing metal substrate. Efforts in this direction have included exploration of several metal and oxide [23] surfaces, as well as manipulation onto thin layers of NaCl [8,11,24]. However, NaCl is not free from intrinsic broadening [25–27]. All in all, the effective decoupling of edge states leading to spin quantum-dot phenomenology is therefore not yet realized.

Inspired by the excellent results of ultra-thin MgO layers as passive support for atoms and molecules [28–31], here we employ MgO monolayers (MgO_{ML}) grown on the (100) surface of a silver single crystal to electronically decouple chiral GNRs. The quantum-well (QW) states confined at the longitudinal edges of finite GNRs (2 to 12 nm) display an exceptionally small intrinsic linewidth of 1 meV. Charge transfer from Ag(001) across the MgO ML takes place in integer number of electrons, leading to the alternation of odd and even electron occupation of the QW states as the GNR length increases, with an average n-type doping of $\sim 1.5 \text{ e}^-/\text{nm}$. The MgO spacer also enhances electron-electron (e-e) interactions that stabilize odd occupations with correlation gaps of ~ 50 to 100 meV between singly occupied and singly unoccupied QW states. This is the signature of a spin-1/2 state associated to odd numbers of electrons in the mean-field-Hubbard (MFH) approximation. Our MFH simulations also show that the MgO spacer preserves Coulomb e-e interactions of gas-phase GNRs. This enabled a pseudo “gating” effect, in which the addition of a single molecular

precursor unit (PU) can affect the odd/even occupancy of the GNR.

RESULTS AND DISCUSSION

Chiral graphene nanoribbons (m,n,w)-GNRs grow with their longitudinal axis along a vector (m, n) of the graphene lattice, enclosing w C-C pairs among them. In this notation, the edge is defined as an alternating sequence of n arm-chair and $m-n$ zig-zag segments (Fig. 1a). Here we work with (3,1,8)- and (3,2,8)-GNRs. To accommodate their chiral vectors, these ribbons alternate three zig-zag edge segments with arm-chair ones. As a consequence, they exhibit edge states and a symmetry-protected topological (SPT) energy gap, giving rise to zero-energy SPT end states at their termini [9]. Both edge and SPT states can host spins with different degree of delocalization in the presence of electronic correlations. However, on the rather electrophilic substrate like Au(111) and the related intermetallic surface GdAu_2 , we found slight doping of holes and electrons respectively [9,20], with negligible correlation gaps. The origin of this is generally attributed to the suppression of e-e interactions due to screening by the surface electrons. Consequently, only a weak spin polarization is expected. In fact, on GdAu_2 , a small spin polarization amounting to less than 8% was determined by spin polarized STM [20].

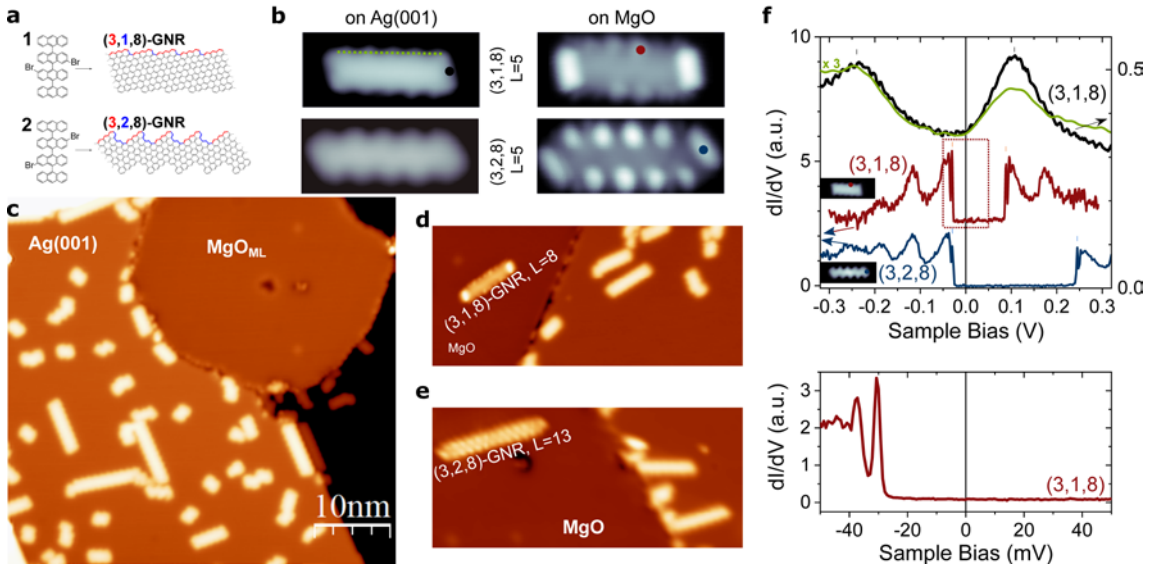


Figure 1.- STM characterization of $(3,n,8)$ -GNRs on MgO/Ag(001). **a**) Chemical structures of the precursors and the resulting (3,1,8)- and (3,2,8)-GNRs. **b**) STM topography ($V_b = 0.5$ V, $I_t = 10 - 70$ pA, image width 6 nm) of (3,1,8) (upper row) and (3,2,8) (bottom row) GNRs with $L=5$ precursor units length on Ag(001) and on $\text{MgO}_{\text{ML}}/\text{Ag}(001)$. **c**) STM image ($V_b = 0.5$ V, $I_t = 50$ pA) of a MgO_{ML} island coexisting with GNRs synthesized over the regions of bare Ag(001). **d,e**) Instances of successful atomic manipulation of GNRs from the Ag surface to the MgO island ($V_b = 0.5$ V, $I_t = 50$ pA). **f**) The top panel shows dI/dV spectra of the $L=5$ (3,1,8) and (3,2,8) GNRs on Ag(001) and on the MgO_{ML} (stabilization $V_b = 0.5$ V, $I_t = 100$ pA, $V_{\text{mod}} = 1$ mV and 8 mV r.m.s. for spectra on MgO and Ag(001) respectively). The colour code indicates the positions in panel (b) where the spectra were acquired. Insets show the in-gap ($V_b = 5$ mV) constant-height tunnelling current image of the corresponding GNRs in panel (b). The green curve is an average of spectra taken along the dashed line in panel (b). The bottom panel shows a high resolution dI/dV spectrum within the region enclosed by the dotted rectangle (stabilization $V_b = 0.5$ V, $I_t = 200$ pA and $V_{\text{mod}} = 0.4$ mV r.m.s.).

We synthesized $(3,n,8)$ -GNRs on Ag(001) by thermally activated Ullmann coupling and subsequent cyclodehydrogenation of precursors 1 and 2 [9,20], leading to GNRs with $n=1$ and 2, respectively (see Fig. 1a and Supplementary Fig. S1) with varying lengths between $L=2$ to 22 precursor units (PU). High-resolution constant height current images (Supplementary Fig. S1) with CO-functionalized tips confirm the correct structure of the GNRs. Differential conductance (dI/dV) spectra on the GNRs over the Ag(001) surface display a set of broad peaks around the Fermi level (Figure 1f for $n=1$ and $L=5$) that, in anticipation to our later results, can be assigned to QW states stemming from the confinement of the conduction band state localized at the edges. The typical full-width at half-maximum (FWHM) of these resonances varies from ~ 50 meV to 100 meV (see Fig. 1f and Supplementary Fig. S2).

The GNRs were transferred to the previously grown MgO monolayer patches by means of lateral manipulation with the STM tip (see Fig. 1c-e and Supplementary Fig. S2). The GNRs over the MgO island exhibit a distinct change in STM topographic images (Fig. 1b) and, more importantly, the electronic structure changes drastically. As shown in Fig. 1f for $n=1,2$ and $L=5$, the molecular resonances are much sharper, featuring linewidths of the order of 1 meV (Supplementary Fig. S3a illustrates how it is determined). Each resonance appears followed by two satellite peaks at 8 and 77 mV distance (independently of the GNR length) that correspond to the excitation of Frank-Condon resonances (Supplementary Fig. S3b), in analogy with previous studies of individual molecules and GNRs weakly coupled to metal surfaces [32,33].

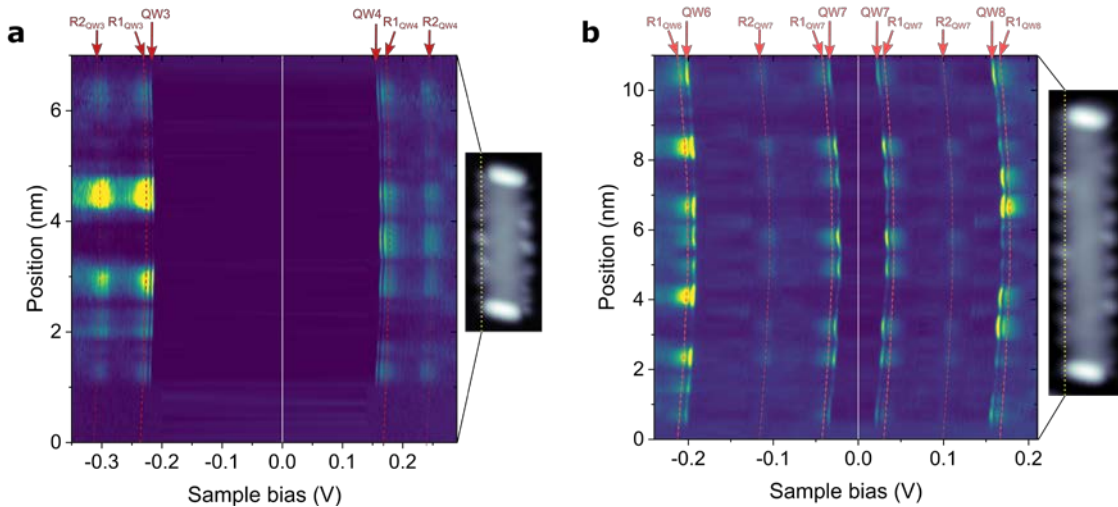


Figure 2.- Detailed electronic structure of edge state in GNRs/MgO. Stack plots of dI/dV spectroscopy curves taken along the chiral edge of $(3,1,8)$ -GNRs with $L=6$ (a) and $L=11$ (b). Insets show topography images ($V_b=0.5$ V, $I_t=50$ pA). Dotted yellow lines indicates the positions where spectroscopy was retrieved. Spectroscopy parameters: stabilization $V_b=0.5$ V and $I_t=200$ pA, $V_{mod}=1$ mV rms, $T=1.2$ K and 4.3 K for panel (a) and (b) respectively. n^{th} order QW states are labelled as QWn. Reddish dashed lines are a guide to the eye of the position dependent energy of their associated Frank-Condon resonances (Rm_{QWn} : m^{th} replica of the n^{th} QW state, see Supplementary Fig. S3b).

To elucidate the orbital character of the sharp GNR resonances on MgO, we acquired dI/dV spectroscopy curves along the GNRs edges. Figs. 2a and 2b show stacked spectroscopy plots as a function of bias and position along the edge for $(3,1,8)$ -GNRs with $L=6$ and 11, respectively. In $L=6$ (Fig. 2a and 3a) we observe two QW states (each one flanked by their Frank-Condon replica) separated by a large energy gap of 380 meV. Their spatial

distribution shows conductance maxima distributed along the edge, with different number and position of nodal planes on either side of the Fermi level. In the case of $L=11$, there are four different QW states within the same energy window (Fig. 2b and 3b), what is consistent with the larger GNR length. Notably, for $L=11$, the frontier QW states around the Fermi level exhibit identical intensity profiles along the edge. This suggests that the energy gap of each of these GNRs has a different origin.

We identify the orbitals associated with the resonances on both Ag(001) and MgO_{ML} by comparing in Fig. 3a,b their experimental spatial distribution with MFH calculations of the local density of states (LDOS) (see Methods). For $L=6$ on Ag(001) the experiments resolve an occupied state at -42 mV and a fully unoccupied state at 245 mV. For this GNR, MFH results for the LDOS of the 3rd and 4th QW states reproduce the experimental dI/dV maps of both peaks (Fig. 3a, right). Taking into account that each QW state can accommodate two electrons (with opposite spin), plus two additional electrons in the SPT state (one at each ribbon end), we conclude that this ribbon hosts a fractional charge state of slightly less than $q=8 e^-$ excess electrons relative to the charge-neutral case. Note that the 3rd QW state is still partially unoccupied due to Fermi level pinning. When the GNR is transferred onto the MgO island, all states experience an energy downshift, whereas their intensity distribution still corresponds to the LDOS of the same QW states (Fig. 3a). The 3rd QW state shifts down to -216 mV, and the 4th QW state appears at 163 mV. Therefore, the GNR retains approximately the same occupancy, although in this case, the charge doping is exactly $q=8 e^-$, because there is no in-gap spectral weight. As sketched in Fig. 3a, the n-doping on the oxide layer is a consequence of the reduced work function of MgO/Ag(001) relative to the bare Ag(001) [34], which we have determined as $\delta\Phi_{[\text{Ag-MgO}]}=0.7 \text{ eV}$ from the analysis of their respective field emission resonances (see Supplementary Fig. S4).

The extremely narrow lineshape of the molecular resonances on MgO, and the appearance of FC resonances that require transitions to long-lived excited molecular states [32], points to a very efficient electronic decoupling from the metal substrate. In this context, one would expect enhanced e-e interactions [8,31]. This is the case of the (3,1,8)-GNR with $L=11$ shown in Fig. 3b, which displays a qualitatively different behaviour than the $L=6$ case. On Ag(001) we find a partially occupied state at -23 mV and a fully unoccupied state at 123 mV. MFH simulations (see also Supplementary Fig. S5) reveal that they correspond to the 6th and 7th QW states. Taking into account the two additional electrons hosted by the SPT state, we conclude a charge state of slightly less than $q=14 e^-$. On MgO, all states experience again an energy downshift. The 6th QW state shifts in energy down to -200 mV. The 8th QW state, which was barely resolved on Ag(001) at around 250 mV, is now prominent at 171 mV. Remarkably, the 7th QW appears split in two states with identical spatial distribution at -30 mV and 27 mV. Since only one of them is occupied, we conclude an odd occupancy of exactly $q=15 e^-$, which implies one singly occupied and one singly unoccupied frontier state with opposite spin, as depicted by the arrows in Fig. 3b.

The work function reduction in the MgO ($\delta\Phi_{[\text{Ag-MgO}]}$, see Supplementary Fig. S4) acts here as a gating potential for the QW states (Supplementary Table S1 and Fig. S6) [34]. We represent its associated energy downshift in Figs. 3a,b by dashed grey vertical arrows. Many-body correlations are taken into account in the MFH model by the on-site Coulomb repulsion, U . Its effect for the 7th QW state of $L=11$ at half-filling as U increases is to induce a splitting of the two spin channels (experimental value in Fig. 3b of $\sim 50 \text{ meV}$). Due to the

confinement of the flat edge state band[9,35], if the 7th QW state is sufficiently close to the Fermi level for $U=0$, small U values will cause the population of one additional state with one electron from the Ag(001) reservoir of a given spin quantum number, leaving an unoccupied state with opposite spin. Within the MFH model, this leads to a total spin- $\frac{1}{2}$ distributed as depicted by the simulation of the spin density shown in Fig. 3c. In contrast, for $L=6$, e-e correlations ($U>0$) renormalize the eigenenergies (~ 10 meV for $U=3$ eV), but the highest occupied molecular state remains deep below the Fermi level, making the double occupancy (i.e. closed shell configuration) energetically favourable and rendering a non-magnetic ground state.

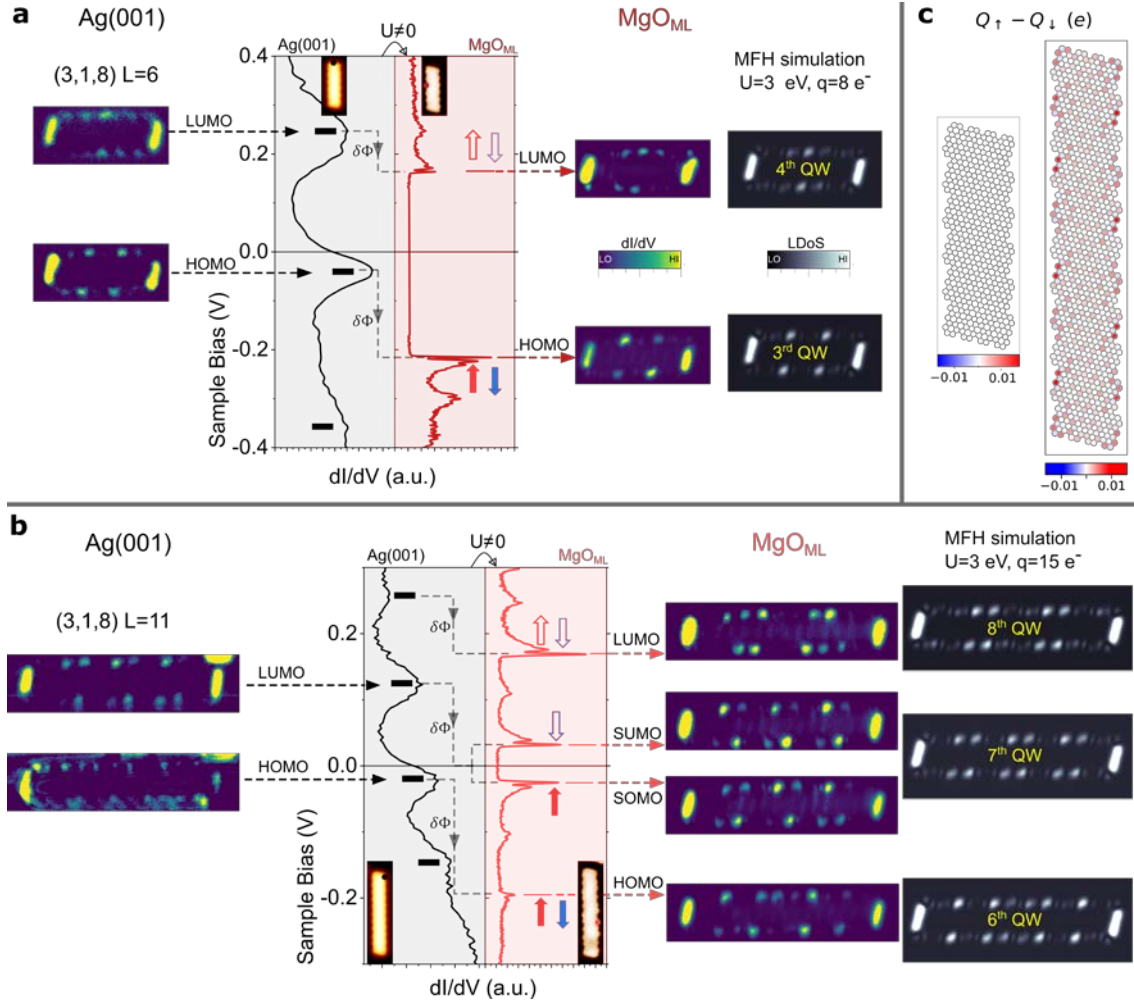


Figure 3.- Even/odd occupancy of discrete QW states in (3,1,8)-GNRs. (a,b) dI/dV point spectra of $L=6$ and 11 GNRs respectively taken at the positions marked in the insets. Images on the left column are experimental constant current dI/dV maps at the indicated energies on Ag(001). Images on the right column are constant height dI/dV maps on MgO_{ML} and theoretical LDOS simulations (see Methods) of the QW states indicated by the yellow labels. Black[red] dashed arrows indicate the energy at which the different QW states appear on Ag(001)[MgO_{ML}], connecting the spectroscopic features with their corresponding maps. For $L=11$ (b), the 6th QW state is close enough to the Fermi level so that the finite U plays a significant role, splitting the two spin channels. The red/blue filled[empty] arrows represent the spin of the single electron occupied[unoccupied] states. **(c)** Calculated MFH spin polarization projected on the C sites (see Methods) for $L=6$ and $L=11$ GNRs with $U=3.0$ eV and charge states of 8 and 15 electrons, respectively. STM parameters: Insets in (a) and (b) display the topography at $V_b=0.5$ V and $I_t=50$ pA in the case of Ag(001) and constant height in-gap current at $V_b=2$ mV in the case of MgO_{ML} . dI/dV spectroscopy parameters in (a) and (b): stabilization at 0.5 V/100 pA ($V_{mod}=5-8$ mV) for

Ag(001) and 0.5 V/200 pA ($V_{\text{mod}}=1$ mV) for MgO_{ML}. Parameters for dI/dV mapping: on Ag(001) constant current maps are taken at $V_b/I_t=210$ mV/200 pA (QW4) and -72 mV/200 pA (QW3) with $V_{\text{mod}}=5$ mV for $L=6$ (a), and 123 mV/100 pA (QW7) and -30 mV/100 pA (QW6) with $V_{\text{mod}}=8$ mV for $L=11$ (b); constant height maps on MgO_{ML} are taken after opening the feedback at the GNRs' centre with regulation set points of -200 mV/200 pA (QW4) and 150 mV/150 pA (QW3) with $V_{\text{mod}}=1$ mV for $L=6$ (a), and of 50 mV/20[100/5] pA (QW8[QW7/QW6]) with $V_{\text{mod}}=1$ mV for $L=11$ (b). $T=1.2$ K

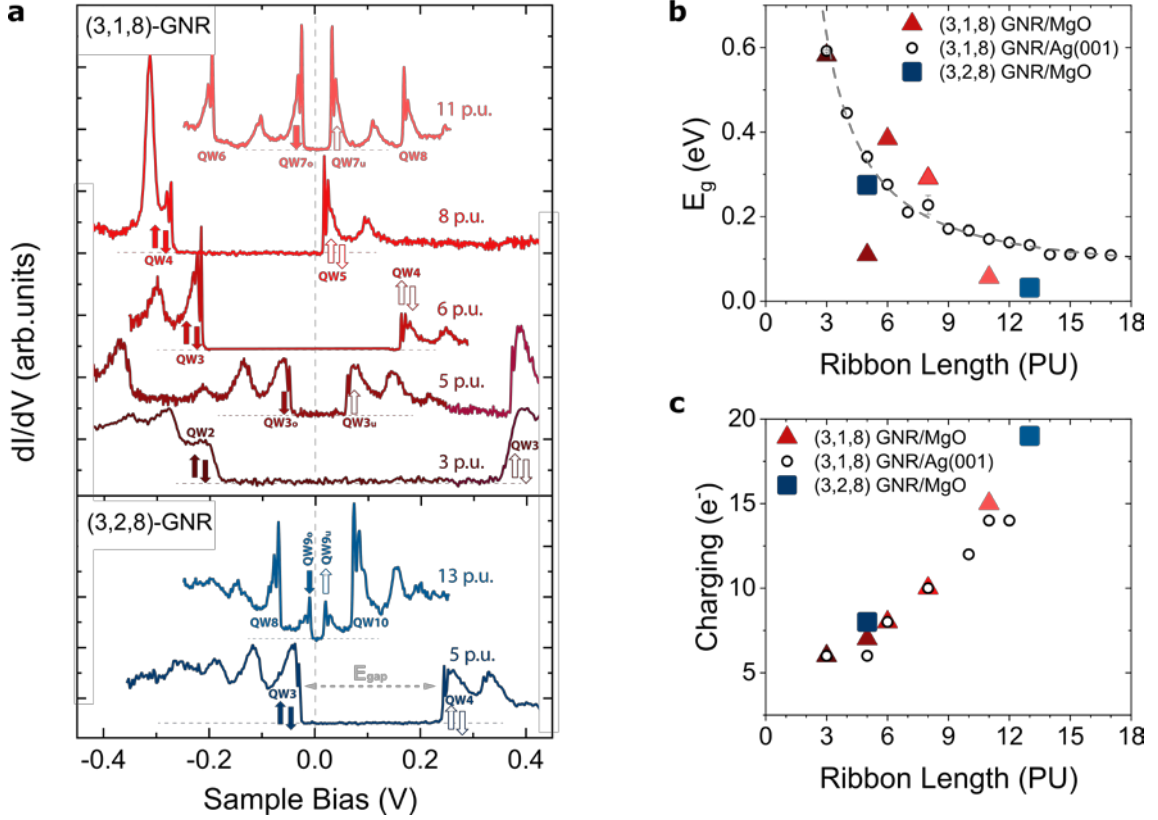


Figure 4.- Energy gap across the Fermi level in $(3,n,8)$ -GNRs repositioned on MgO_{ML}. a) Waterfall plot of dI/dV spectra (stabilization at $V_b = 0.5$ V, $I_t = 200$ pA; $V_{\text{mod}} = 1$ mV r.m.s.; $T=1.2$ K for $n=1$ and 4.3 K for $n=2$) of several $(3,n,8)$ -GNRs showing the non-monotonous behaviour of the gap across the Fermi level. The acquisition position in the case of the $n=8$ and $L=6,11$ is shown in the insets of Figs. 3a,b. Filled/empty arrows represent occupied/unoccupied single electron states with well defined S_z quantum number. b) Evolution of the gap as a function of the GNR length of $(3,1,8)$ -GNRs on Ag(001) –empty circles, error bars are derived from measurements in 2 or 3 GNRs of the same length– and several representative examples of $(3,1,8)/(3,2,8)$ -GNRs on MgO_{ML} –triangles/squares–. The dashed line is an asymptotic fit proportional to $L^{-3/2}$. c) Exact charge state of $(3,1,8)/(3,2,8)$ -GNRs on MgO monolayer and approximate charge state of $(3,1,8)$ -GNRs on Ag(001), see Supplementary Table S1 for further details

All $(3,1,8)$ - and $(3,2,8)$ -GNRs investigated here can be classified into the two categories shown in Figure 3, i.e., either odd occupation with identical QW states around the Fermi level, or even occupation with different QW states (see Supplementary Fig. S5). Figs. 4a and 4b illustrate an interesting anomaly in the gap across the Fermi level (E_g) of $(3,n,8)$ -GNRs on MgO: its size does not vary monotonically as a function of length. For instance, the gap for $n=1$ and $L=5$ is about 100 meV, whereas for just one more PU ($L=6$) the gap increases abruptly to ~ 400 meV, to experience again a substantial drop between $L=8$ ($E_g \sim 300$ meV) and $L=11$ ($E_g \sim 50$ meV). This is in contrast with the evolution of the GNRs' gap on Ag(001), which follows the expected asymptotic decay with increasing length of a particle-in-a-box (Fig. 4b and Supplementary Fig. S2). On MgO, some $(3,n,8)$ -GNRs exhibit similar gaps to the

ones on Ag(001), while others have a much reduced value. Fig. 4c shows the excess charge (q) in all GNRs determined by means of the same procedure as for $L=6$ and $L=11$ GNRs with $n=1$ above. The anomalously small values of E_g (Figs. 4b,c) are univocally linked to frontier states with identical spatial distribution (see Supplementary Fig. S5) and, hence, to odd occupations. These GNRs have, thereby, open-shell character of the edge state and non-zero total spin.

To address this scenario, we developed a theoretical model accounting for electron doping as a function of length and chirality. When molecular species lie on substrates with work function Φ lower than their electron affinity E_a , an interfacial charge redistribution takes place, resulting in the electron accumulation into unoccupied molecular states and the build-up a local interface dipole with associated potential energy U_d that opposes to charge transfer [35–37]. In equilibrium, the chemical potential (μ) at the metal's Fermi level and the charge state of the molecule is determined by the shift of μ from the value at which the molecule retains charge neutrality, μ_0 (Fig. 5a).

$$\Delta\mu = \mu - \mu_0 = E_a - \Phi - U_d \quad (1)$$

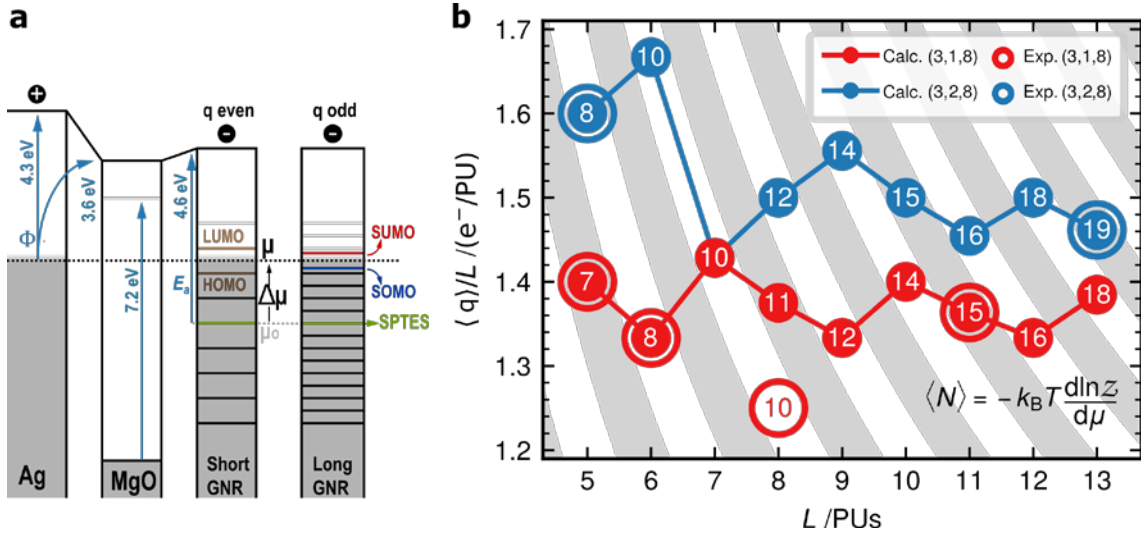


Figure 5.- Comparison of experimental electron occupation and theoretical calculations. a) Energy level alignment scheme for short even- and long odd-integer charged GNRs on top of a MgO layer (band gap 7.2 eV [42]), respectively. The neutral level of the GNRs is referenced by the binding energy of the two symmetry-protected topological end states (SPTES). **b)** Fit of the grand canonical charging model to the experimentally observed charge per precursor unit as a function of ribbon length for the two types of chiral GNRs. Stripes in grey correspond to odd-integer excess charge.

Since the Ag(001) work function ($\Phi_{\text{Ag}(001)}=4.3$ eV [31,36,38]) is smaller than the GNR's electron affinity (comparable to the bulk work function of graphene, $\Phi_{\text{GNR}}\sim 4.61$ eV), the nanoribbons exhibit significant n-doping already on Ag(001). As shown in Supplementary Table S1, we find an average doping of 1.25 e^- / PU for (3,1,8)-GNR on Ag(100), in close agreement with the previous reported value of 1.3 e^- / PU on a similar system [39]. The addition of a MgO insulating layer further reduces the substrate's work function via the pillow effect [31,40,41] by $\delta\Phi\sim 0.7$ eV (see Supplementary Fig. S4), to yield an exceptionally low work function $\Phi_{\text{Ag/MgO}}\sim 3.6$ eV. The MgO also suppresses wave-function overlap between molecule and metal such that only integer charges are allowed. Depending on the alignment of μ with respect to the discrete molecular levels (Fig. 5a), the resulting charge

state may be either even or odd. Furthermore, the dielectric spacer reduces the interface capacitance between molecule and metal, and thereby the charge state.

To extract the magnitude and parity of the acquired excess charge (q), we represent each GNR in contact with the substrate bath by a chemical potential μ and temperature T in the grand canonical ensemble. We compute the internal energy of the various charge states of (3, n ,8)-GNRs ($n=1,2$) with increasing length L using the MFH model (see Supplementary Theoretical Methods) and obtain the mean number of excess electrons $\langle q \rangle$ for any given chemical potential μ (see Supplementary Fig. S7) via the relation

$$\langle q(\mu, L, T) \rangle = -k_B T \frac{dZ(\mu, L, T)}{d\mu} \quad (2)$$

where $Z(\mu, L, T)$ is the grand canonical partition function obtained by summing over all relevant charge states for each GNR (See Supplementary Theoretical Methods).

Our model reproduces that for a fixed chemical potential the excess charge increases with length. In fact, the addition of one additional PU increases q by either zero, one or two electrons, very much in line with the experimental observation of a non-integer mean value of q/L . This is due to the intrinsic evolution of the level spacing of the QW edge states of (3, n ,8)-GNR with length and chirality. In the thermodynamic limit $L \rightarrow \infty$, $\langle q \rangle / L$ asymptotically approaches the intensive value corresponding to the n-type carrier density of a one dimensional GNR gated by an electric potential $\Delta\mu/|e|$.

To obtain the local gating $\Delta\mu$ of each family of chiral ribbons on the MgO layer, we fit the experimental electron doping deduced in Figs. 3 and 4 with predicted charges using $\Delta\mu$ as a length-independent free parameter. The results of the fit, shown in Fig. 5b, reproduce the charging pattern of (3,1,8)- and (3,2,8)-GNRs with $\Delta\mu=0.51$ eV and 0.49 eV, respectively (see Supplementary Figure S7 for details). The only experimental deviation is the case of (3,1,8)-GNR with $L=8$, for which the model predicts the single occupancy of the 5th QW state. Instead, this GNR appears on MgO charged with ten electrons, with its LUMO (the 5th QW state) at only 17 meV above E_F (Fig. 4a and Supplementary Fig. S5), i.e., at the verge of single occupancy. This is likely due to the electrostatic potential emanating from nearby charged defects in the MgO lattice (see examples in Supplementary Figs. S8 and S9).

The determined $\Delta\mu$ value is about half of the ~ 1 eV work function difference between MgO/Ag(001) and graphene. This can be attributed to the existence of a sizable interface dipole across the MgO layer, which conversely acts to lower the GNR's charge state [37]. From equation (1), the electrostatic energy stored in the interface becomes $U_d \sim 0.5$ eV, which matches well with a plate capacitor model [37] with excess charge lying mainly on the zig-zag edges of the GNRs.

CONCLUSION

When chiral GNRs are positioned on the MgO monolayer on Ag(001), the combination of its low work function and the electronic decoupling gives rise to quantized charge transfer to their edge states, whose occupation can be controlled by a modification of the length of just one PU. As a consequence, the Fermi level raises up to QW states that lie 300 to 500 meV above in the corresponding charge neutral GNR. Furthermore, the e-e correlations of

extended GNR edge states on MgO are sufficiently large as to stabilize singly occupied QW edge states, leading to spin-1/2 quantum dot behaviour at the MFH level of theory, with spin-split frontier states. This is analogous to the behaviour of single electron transistors in semiconducting quantum dots, where the dot occupancy is controlled by the GNR length instead of by a gate voltage. It opens up possibilities for disruptive functional devices such as graphene-based spin qubits and fully spin-polarized field effect transistors.

The extreme sensitivity of charge doping to the length and the chirality suggests that an external electric field could also be utilized to regulate the number of electrons and their energy alignment with respect to the Fermi level. Actually, we find that the energy landscape determined by the electrostatic potential at the tip-sample gap can induce rigid shifts of the whole GNR spectrum of the order of tens of meV (Figs. 2a, 2b and Supplementary Fig. S8), or even switching between odd and even occupancy (Supplementary Figure S9). Such control capability can be combined with atomic manipulation of the GNRs, allowing for the design of artificial arrangements of interacting quantum dots with controllable spin and charge states.

METHODS

Sample preparation. Samples are prepared at a base pressure of 1×10^{-10} mbar. The Ag(001) single crystal from SPL B.V. was cleaned by repeated Argon sputtering and annealing processes at 430 °C. MgO monolayer patches are grown by depositing Mg from a crucible (MBE Komponenten GmBh effusion cell) heated at 320 °C onto the clean Ag(001) held at a constant temperature of 390-400 °C in an O₂ partial pressure of 1×10^{-6} mbar. The growth rate of MgO under these conditions fluctuates between 0.5 to 0.1 ML/min. After deposition, we wait a time lapse of 30 min to properly pump down the residual O₂ molecules in the chamber ($p < 1 \times 10^{-9}$ mbar), and then we anneal the sample during 20 min at 390 °C with the purpose of healing the disorder at the edges of the MgO and decrease the number of point defects within the islands. To synthesize the (3,*n*,1)-GNRs we sublime onto the Ag(001) surface (already with the MgO patches on it) the precursor reactants **1** and **2** (Fig 1a) that yield GNRs with $n=1$ and $n=2$ respectively and then perform a single annealing step at 345 °C during 15 min to achieve full cyclodehydrogenation of the GNRs (further details in Supplementary Experimental Methods). The synthesis and quality of the GNRs on Ag(001) with and without coexisting MgO monolayer islands is the same, with the only exception that in the presence of MgO, the GNRs are in average shorter, probably owing to the lower mobility of the shorter precursor oligomers on the surfaces with lower available metallic area.

Scanning Tunnelling Microscopy and Spectroscopy. All measurements have been performed at the SPECS-JT-STM of the Laboratory for Advanced Microscopy (University of Zaragoza). The whole system operates under ultra-high-vacuum conditions (1×10^{-10} mbar). The tip is grounded and the tunnelling bias V_b is applied to the sample. Data has been taken at $T=1.2$ K unless stated otherwise. Differential tunnelling conductance dI/dV is acquired using a lock-in amplifier at a frequency of 973 Hz and r.m.s. modulation given by V_{mod} . STM images and dI/dV maps were taken either in constant height or in constant current mode, using a stabilization distance determined by the set point indicated at the corresponding caption for each data set. Tips are prepared by electrochemical etching of W wires and subsequent

field emission cleaning (120 V, 1 μ A, 30 min) at the STM head. CO functionalization of the tip is achieved by controlled approach of the tip to a CO adsorbed on the surface at $|V_b| < 5$ mV until a sudden jump in the current is detected.

Mean-field Hubbard calculations. The electronic structure and magnetic ground state of GNRs is well captured by the Hubbard model [43]. By employing a mean-field approach [44], we solve for the ground state and obtain eigen-functions and -energies of the π -electrons, using the same Hamiltonian parametrization as in Refs. [9,20], which has been previously found to reproduce the experimental band gaps in GNRs. We choose a Hubbard parameter of $U = 3$ eV to capture the observed SOMO-SUMO splitting as a function of length and chirality. Differential conductance maps are simulated by squaring a linear combination of p_z orbitals on the lattice at a height of 1.8 nm.

ACKNOWLEDGEMENTS

The authors gratefully acknowledge financial support from the Spanish MCIN/AEI/10.13039/501100011033 and by “ERDF A way of making Europe” through grants PID2019107338RB-C64, PID2019-107338RB-C61, PID2022-138750NB-C21, PID2022-1408450B-C61, PID2020-115406GB-I00, JDC2022-048665-I and the Maria de Maeztu Units of Excellence Program CEX2020-001038-M. This work was also supported by European Regional Development Fund (ERDF) under the program Interreg V-A España-Francia-Andorra (grant no. EFA194/16 TNSI), by the European Union (EU) through the FET-Open project SPRING (863098), the ERC Synergy Grant MoldAM (951519), the ERC-AdG CONSPIRA (101097693), by the Aragon Government (E13-23R and E12-23R), and by the Xunta de Galicia (Centro singular de investigación de Galicia accreditation 2019-2022, ED431G 2019/03 and Oportunius Program).

REFERENCES

- [1] L. Yang, C.-H. Park, Y.-W. Son, M. L. Cohen, and S. G. Louie, *Quasiparticle Energies and Band Gaps in Graphene Nanoribbons*, Phys. Rev. Lett. **99**, 186801 (2007).
- [2] L. Talirz, H. Söde, S. Kawai, P. Ruffieux, E. Meyer, X. Feng, K. Müllen, R. Fasel, C. A. Pignedoli, and D. Passerone, *Band Gap of Atomically Precise Graphene Nanoribbons as a Function of Ribbon Length and Termination*, ChemPhysChem **20**, 2348 (2019).
- [3] Y.-C. Chen, T. Cao, C. Chen, Z. Pedramrazi, D. Haberer, D. G. de Oteyza, F. R. Fischer, S. G. Louie, and M. F. Crommie, *Molecular Bandgap Engineering of Bottom-up Synthesized Graphene Nanoribbon Heterojunctions*, Nature Nanotechnology **10**, 156 (2015).
- [4] A. Kimouche, M. M. Ervasti, R. Drost, S. Halonen, A. Harju, P. M. Joensuu, J. Sainio, and P. Liljeroth, *Ultra-Narrow Metallic Armchair Graphene Nanoribbons*, Nat Commun **6**, 10177 (2015).
- [5] Y.-W. Son, M. L. Cohen, and S. G. Louie, *Energy Gaps in Graphene Nanoribbons*, Phys. Rev. Lett. **97**, 216803 (2006).
- [6] N. Merino-Díez, A. Garcia-Lekue, E. Carbonell-Sanromà, J. Li, M. Corso, L. Colazzo, F. Sedona, D. Sánchez-Portal, J. I. Pascual, and D. G. de Oteyza, *Width-Dependent Band Gap in Armchair Graphene Nanoribbons Reveals Fermi Level Pinning on Au(111)*, ACS Nano **11**, 11661 (2017).
- [7] E. Carbonell-Sanromà et al., *Doping of Graphene Nanoribbons via Functional Group Edge Modification*, ACS Nano **11**, 7355 (2017).

- [8] S. Wang, L. Talirz, C. A. Pignedoli, X. Feng, K. Müllen, R. Fasel, and P. Ruffieux, *Giant Edge State Splitting at Atomically Precise Graphene Zigzag Edges*, Nature Communications **7**, 11507 (2016).
- [9] J. Li, S. Sanz, N. Merino-Díez, M. Vilas-Varela, A. Garcia-Lekue, M. Corso, D. G. de Oteyza, T. Frederiksen, D. Peña, and J. I. Pascual, *Topological Phase Transition in Chiral Graphene Nanoribbons: From Edge Bands to End States*, Nat Commun **12**, 5538 (2021).
- [10] D. J. Rizzo, G. Veber, T. Cao, C. Bronner, T. Chen, F. Zhao, H. Rodriguez, S. G. Louie, M. F. Crommie, and F. R. Fischer, *Topological Band Engineering of Graphene Nanoribbons*, Nature **560**, 204 (2018).
- [11] P. Ruffieux et al., *On-Surface Synthesis of Graphene Nanoribbons with Zigzag Edge Topology*, Nature **531**, 489 (2016).
- [12] N. Merino-Díez et al., *Unraveling the Electronic Structure of Narrow Atomically Precise Chiral Graphene Nanoribbons*, J. Phys. Chem. Lett. **9**, 25 (2018).
- [13] O. Gröning et al., *Engineering of Robust Topological Quantum Phases in Graphene Nanoribbons*, Nature **560**, 209 (2018).
- [14] Q. Sun, R. Zhang, J. Qiu, R. Liu, and W. Xu, *On-Surface Synthesis of Carbon Nanostructures*, Advanced Materials **30**, 1705630 (2018).
- [15] S. Clair and D. G. de Oteyza, *Controlling a Chemical Coupling Reaction on a Surface: Tools and Strategies for On-Surface Synthesis*, Chem. Rev. **119**, 4717 (2019).
- [16] J. Cai et al., *Atomically Precise Bottom-up Fabrication of Graphene Nanoribbons*, Nature **466**, 470 (2010).
- [17] J. Li, S. Sanz, M. Corso, D. J. Choi, D. Peña, T. Frederiksen, and J. I. Pascual, *Single Spin Localization and Manipulation in Graphene Open-Shell Nanostructures*, Nature Communications **10**, (2019).
- [18] D. G. de Oteyza and T. Frederiksen, *Carbon-Based Nanostructures as a Versatile Platform for Tunable π -Magnetism*, J. Phys.: Condens. Matter **34**, 443001 (2022).
- [19] S. Mishra et al., *Topological Frustration Induces Unconventional Magnetism in a Nanographene*, Nat. Nanotechnol. **15**, 22 (2019).
- [20] J. Brede et al., *Detecting the Spin-Polarization of Edge States in Graphene Nanoribbons*, Nat Commun **14**, 6677 (2023).
- [21] J. Fischer, B. Trauzettel, and D. Loss, *Hyperfine Interaction and Electron-Spin Decoherence in Graphene and Carbon Nanotube Quantum Dots*, Phys. Rev. B **80**, 155401 (2009).
- [22] J.-S. Chen, K. J. Trerayapiwat, L. Sun, M. D. Krzyaniak, M. R. Wasielewski, T. Rajh, S. Sharifzadeh, and X. Ma, *Long-Lived Electronic Spin Qubits in Single-Walled Carbon Nanotubes*, Nat Commun **14**, 848 (2023).
- [23] M. Kolmer, A.-K. Steiner, I. Izydorczyk, W. Ko, M. Engelund, M. Szymonski, A.-P. Li, and K. Amsharov, *Rational Synthesis of Atomically Precise Graphene Nanoribbons Directly on Metal Oxide Surfaces*, Science **369**, 571 (2020).
- [24] P. H. Jacobse, M. J. J. Mangnus, S. J. M. Zevenhuizen, and I. Swart, *Mapping the Conductance of Electronically Decoupled Graphene Nanoribbons*, ACS Nano **12**, 7048 (2018).
- [25] W. Steurer, L. Gross, and G. Meyer, *Local Thickness Determination of Thin Insulator Films via Localized States*, Appl. Phys. Lett. **104**, 231606 (2014).
- [26] J. Martinez-Castro, M. Piantek, S. Schubert, M. Persson, D. Serrate, and C. F. Hirjibehedin, *Electric Polarization Switching in an Atomically Thin Binary Rock Salt Structure*, Nature Nanotechnology **13**, 19 (2018).
- [27] J. Repp, G. Meyer, S. Stojković, A. Gourdon, and C. Joachim, *Molecules on Insulating Films: Scanning-Tunneling Microscopy Imaging of Individual Molecular Orbitals*, Physical Review Letters **94**, (2005).
- [28] F. Donati, P. Gambardella, and H. Brune, *Magnetic Remanence in Single Atoms*, Science **352**, 312 (2016).

- [29] F. D. Natterer, K. Yang, W. Paul, P. Willke, T. Choi, T. Greber, A. J. Heinrich, and C. P. Lutz, *Reading and Writing Single-Atom Magnets*, *Nature* **543**, 226 (2017).
- [30] K. Yang, W. Paul, S.-H. Phark, P. Willke, Y. Bae, T. Choi, T. Esat, A. Ardavan, A. J. Heinrich, and C. P. Lutz, *Coherent Spin Manipulation of Individual Atoms on a Surface*, *Science* **366**, 509 (2019).
- [31] M. Hollerer, D. Lüftner, P. Hurdax, T. Ules, S. Soubatch, F. S. Tautz, G. Koller, P. Puschnig, M. Sterrer, and M. G. Ramsey, *Charge Transfer and Orbital Level Alignment at Inorganic/Organic Interfaces: The Role of Dielectric Interlayers*, *ACS Nano* **11**, 6252 (2017).
- [32] G. Reecht, N. Krane, C. Lotze, L. Zhang, A. L. Briseno, and K. J. Franke, *Vibrational Excitation Mechanism in Tunneling Spectroscopy beyond the Franck-Condon Model*, *Phys. Rev. Lett.* **124**, 116804 (2020).
- [33] J. van der Lit, M. P. Boneschanscher, D. Vanmaekelbergh, M. Ijäs, A. Uppstu, M. Ervasti, A. Harju, P. Liljeroth, and I. Swart, *Suppression of Electron-Vibron Coupling in Graphene Nanoribbons Contacted via a Single Atom*, *Nat Commun* **4**, 2023 (2013).
- [34] M. Bielezki, T. Hynninen, T. M. Soini, M. Pivetta, C. R. Henry, A. S. Foster, F. Esch, C. Barth, and U. Heiz, *Topography and Work Function Measurements of Thin MgO(001) Films on Ag(001) by Nc-AFM and KPFM*, *Phys. Chem. Chem. Phys.* **12**, 3203 (2010).
- [35] M. Fahlman, S. Fabiano, V. Gueskine, D. Simon, M. Berggren, and X. Crispin, *Interfaces in Organic Electronics*, *Nat Rev Mater* **4**, 627 (2019).
- [36] M. Willenbockel, D. Lüftner, B. Stadtmüller, G. Koller, C. Kumpf, S. Soubatch, P. Puschnig, M. G. Ramsey, and F. S. Tautz, *The Interplay between Interface Structure, Energy Level Alignment and Chemical Bonding Strength at Organic-Metal Interfaces*, *Phys. Chem. Chem. Phys.* **17**, 1530 (2015).
- [37] P. Hurdax, M. Hollerer, P. Puschnig, D. Lüftner, L. Egger, M. G. Ramsey, and M. Sterrer, *Controlling the Charge Transfer across Thin Dielectric Interlayers*, *Adv. Mater. Inter.* **7**, 2000592 (2020).
- [38] G. N. Derry, M. E. Kern, and E. H. Worth, *Recommended Values of Clean Metal Surface Work Functions*, *J. of Vac. Sci. & Tech. A* **33**, 060801 (2015).
- [39] M. Corso, R. E. Menchón, I. Piquero-Zulaica, M. Vilas-Varela, J. E. Ortega, D. Peña, A. Garcia-Lekue, and D. G. de Oteyza, *Band Structure and Energy Level Alignment of Chiral Graphene Nanoribbons on Silver Surfaces*, *Nanomaterials* **11**, 3303 (2021).
- [40] G. Witte, S. Lukas, P. S. Bagus, and C. Wöll, *Vacuum Level Alignment at Organic/Metal Junctions: "Cushion" Effect and the Interface Dipole*, *Appl. Phys. Lett.* **87**, 263502 (2005).
- [41] H.-J. Freund and G. Pacchioni, *Oxide Ultra-Thin Films on Metals: New Materials for the Design of Supported Metal Catalysts*, *Chem. Soc. Rev.* **37**, 2224 (2008).
- [42] S. Schintke, S. Messerli, M. Pivetta, F. Patthey, L. Libioulle, M. Stengel, A. De Vita, and W.-D. Schneider, *Insulator at the Ultrathin Limit: MgO on Ag(001)*, *Phys. Rev. Lett.* **87**, 276801 (2001).
- [43] J. Hubbard and B. H. Flowers, *Electron Correlations in Narrow Energy Bands III. An Improved Solution*, *Proc. R. Soc. Lond. A* **281**, 401 (1964).
- [44] S. Sanz, N. Papior, G. Giedke, D. Sánchez-Portal, M. Brandbyge, and T. Frederiksen, *Spin-Polarizing Electron Beam Splitter from Crossed Graphene Nanoribbons*, *Phys. Rev. Lett.* **129**, 037701 (2022).

Supplementary Information for:
Engineering open-shell extended edge states in chiral graphene nanoribbons on MgO

Amelia Domínguez-Celorrío^{1,2,3,†}, Leonard Edens^{4,†}, Sofía Sanz⁵, Manuel Vilas-Varela⁶, Jose Martinez-Castro⁷, Diego Peña⁶, Véronique Langlais⁸, Thomas Frederiksen^{5,9}, José I. Pascual^{4,9}, and David Serrate^{1,10,11*}

¹Instituto de Nanociencia y Materiales de Aragón (INMA), CSIC-Universidad de Zaragoza, Zaragoza, E-50009, Spain

²School of Physics and Astronomy, Monash University, Clayton, VIC 3800, Australia

³ARC Centre for Future Low Energy Electronics Technologies, Monash University, Clayton, VIC 3800, Australia

⁴CIC NanoGUNE BRTA, San Sebastián, E-20018, Spain

⁵Donostia International Physics Center, San Sebastián, E-20018, Spain.

⁶Centro Singular de Investigación en Química Bilóxica e Materiais Moleculares (CiQUS) and Departamento de Química Orgánica, Universidade de Santiago de Compostela, Santiago de Compostela, E-15782, Spain.

⁷Peter Grünberg Institut (PGI-3), Forschungszentrum Jülich, 52425 Jülich, Germany

⁸Centre d'Elaboration de Materiaux et d'Etudes Structurales, CNRS, Toulouse, F-31055 France

⁹Ikerbasque, Basque Foundation for Science, Bilbao, E-48013, Spain.

¹⁰Departamento de Física de la Materia Condensada, Universidad de Zaragoza, Zaragoza, E-50009, Spain

¹¹Laboratorio de Microscopias Avanzadas (LMA), Universidad de Zaragoza, Zaragoza, E-50018, Spain.

†These authors contributed equally

*email: serrate@unizar.es

Table of Contents:

1. Supplementary Experimental Methods.
2. Extended Spectroscopy Data.
3. Supplementary Theoretical Methods.
4. Electrostatic gating of chiral graphene nanoribbons on MgO.
5. Supplementary References.

1. Supplementary Experimental Methods

(3, n ,1)-GNRs synthesis starts by sublimating precursors **1** and **2** (Figure S1a and S1e) onto the Ag(001) surface where MgO monolayer (MgO_{ML}) patches have been previously grown, for $n=1$ and $n=2$ respectively. Ullmann coupling of precursor **1** takes place at room temperature as they reach the Ag(001) surface. As shown in Fig. S1b, the precursor units assemble as short oligomers, mostly attached to the edges of Ag terraces. Upon annealing to 300 °C (Figure S1c), we distinguish a clear change in the morphology of the sample with longer and ordered chains in islands. The distance between the protrusions shown in Figure S1c is 8.7(1) Å, which corresponds with the expected periodicity of poly-(**1**) chains. Mild annealing processes of poly-(**1**) samples above 300 °C led to partial cyclodehydrogenation (CDH) of the polymeric chains (Fig. S1c). Fully planarized (3,1,8)-GNRs form after 15 minutes at 345 °C (Fig. S1d).

Similarly, as illustrated by Fig. S1e, precursor **2** also undergoes Ullmann coupling on Ag(001) at room temperature. In this case, densely packed and ordered poly-(**2**) chains appear without any additional annealing for sufficiently large coverages (as in the left side terrace of Fig. S1f). The characteristic period of these chains is 10.9(1) Å, which corresponds with the expected periodicity of poly-(**2**) chains (Fig. S1g). Annealing of poly-(**2**) samples at 345 °C during 15 minutes led, as in the case of precursor **1**, to a complete CDH and the formation of (3,2,8)-GNRs (Fig. S1h).

The synthesis and quality of the GNRs on Ag(001) with and without coexisting MgO_{ML} islands is the same, with the only exception that in the presence of MgO, the GNRs are in average shorter, probably owing to the lower mobility of the shorter precursor oligomers on the surfaces with lower available metallic area.

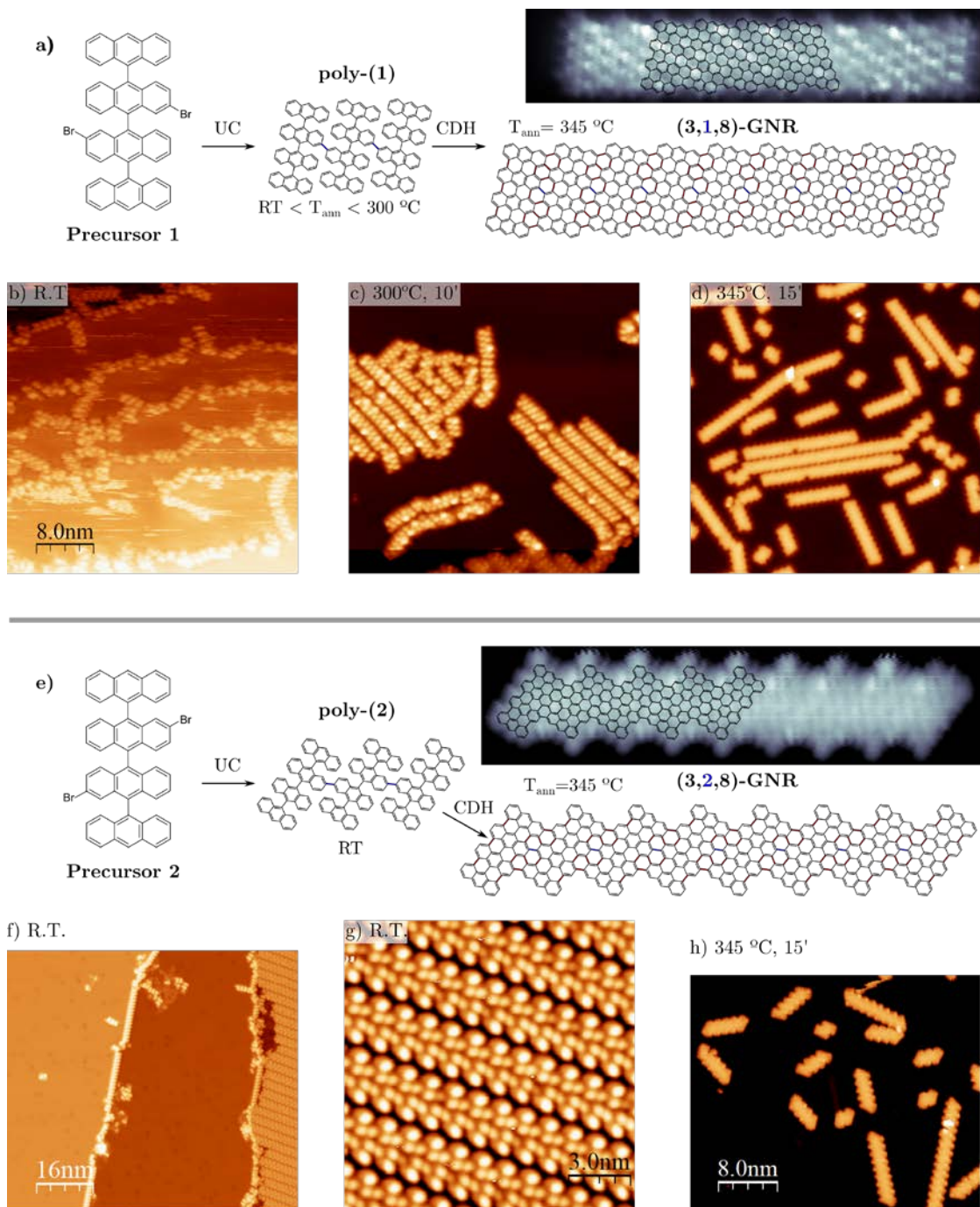


Figure S1.- On-surface synthesis of $(3,n,8)$ -GNRs on Ag(001) for $n=1$ (a-d) and $n=2$ (e-h). Panels (a) and (e) show the reaction schemes of precursors **1** and **2** respectively showing that Ullmann polymerization takes place already at room temperature, and that short annealing of the polymeric chains at 345 °C gives rise to a complete cyclodehydrogenation (CDH) in both cases. Regulation V_b of STM topographies is 0.5 V in panels (b-d) , 1.8 V in panel (f), 0.05 V in panel (g), and 0.5 V in panel (h). High resolution insets in (a) and (e) are constant height tunnelling current images with functionalized tips taken at 1.5 mV and 500 mV for $(3,1,8)$ - and $(3,2,8)$ -GNRs respectively.

2. Extended spectroscopy data.

Figure S2 shows, for (3,1,8)-GNRs on Ag(001), the gradual closing of the gap between the first fully unoccupied quantum well (QW) state and the immediately preceding in energy QW state. As the energy spacing between adjacent QW states decreases for increasing length L , the associated dI/dV resonances become slightly narrower. STM images on the left side of Fig. S2 illustrate the distinct change in apparent shape of the GNRs as they are stepwise introduced onto the MgO_{ML} patch.

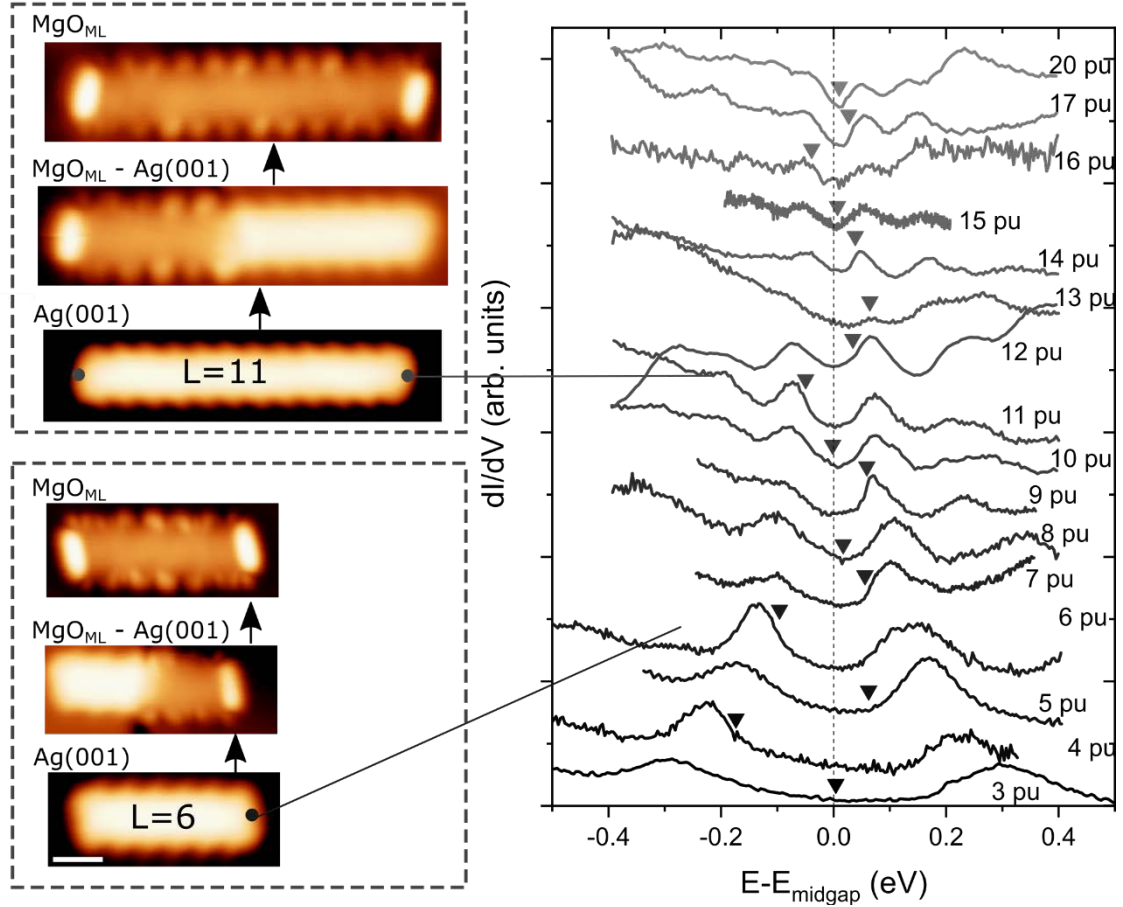


Figure S2.- dI/dV spectra of (3,1,8)-GNRs on Ag001 for several lengths. Topography and spectroscopy stabilization set points are 0.5 V and 50 pA. Lock-in modulation 5 mV r.m.s. Spectra have been vertically offset and normalized for the sake of clarity. In the abscissa axis we represent the energy difference with respect to the midgap energy, E_{midgap} , rather than the traditional convention of referring energy with respect to Fermi level. E_{midgap} is defined as the middle point between the central energy of the first unoccupied (or partially unoccupied) state and that of the immediately preceding state in energy. The experimental Fermi level in each spectrum is indicated by triangles. In this way, the evolution of the gap between QW states nearest to Fermi level can be better appreciated. The left column shows topography images of (3,1,8)-GNRs on Ag(001) with $L=6$ and 11 and, subsequently in the vertical direction, the same GNRs after lateral manipulation: partially and fully inserted in the MgO_{ML}. The black circles mark the position where the corresponding dI/dV spectra were acquired. The spectra of the other ribbons were also taken at the arm-chair termini, where all QW states feature some intensity. Nevertheless, QW states at the same set of energies can be detected along the chiral edge, though they are often much less intense and not all of them manifest in the same position as a consequence of their intrinsic intensity pattern.

One of the most striking changes observed on the MgO is the extremely low linewidth of the QW resonances. We have studied their full width at half maximum (FWHM) and the results are presented in Fig. S3a. At the lowest experimental temperature $T=1.13$ K the linewidth of the 3rd QW state of $L=5$ (3,1,8)-GNR decreases down to 1.5 mV as the lock-in modulation amplitude is reduced stepwise to values smaller than $k_B T/|e|\sim 0.1$ mV. As discussed in the main text, these sharp resonances are always accompanied by broader peaks that appear at 8 mV and 80 mV (see Fig. S3b). This separation is constant throughout the GNR and independent of its length. Constant height dI/dV maps of the principal resonance (P, the sharp one) and their replicas (R) unveil that they have identical spatial distribution (Fig. S3b). This overall behaviour is characteristic of vibrational Franck Condon resonances excited as a consequence of long lived ionic GNR states as electrons or holes are injected into the QW states during the tunnelling process [1,2].

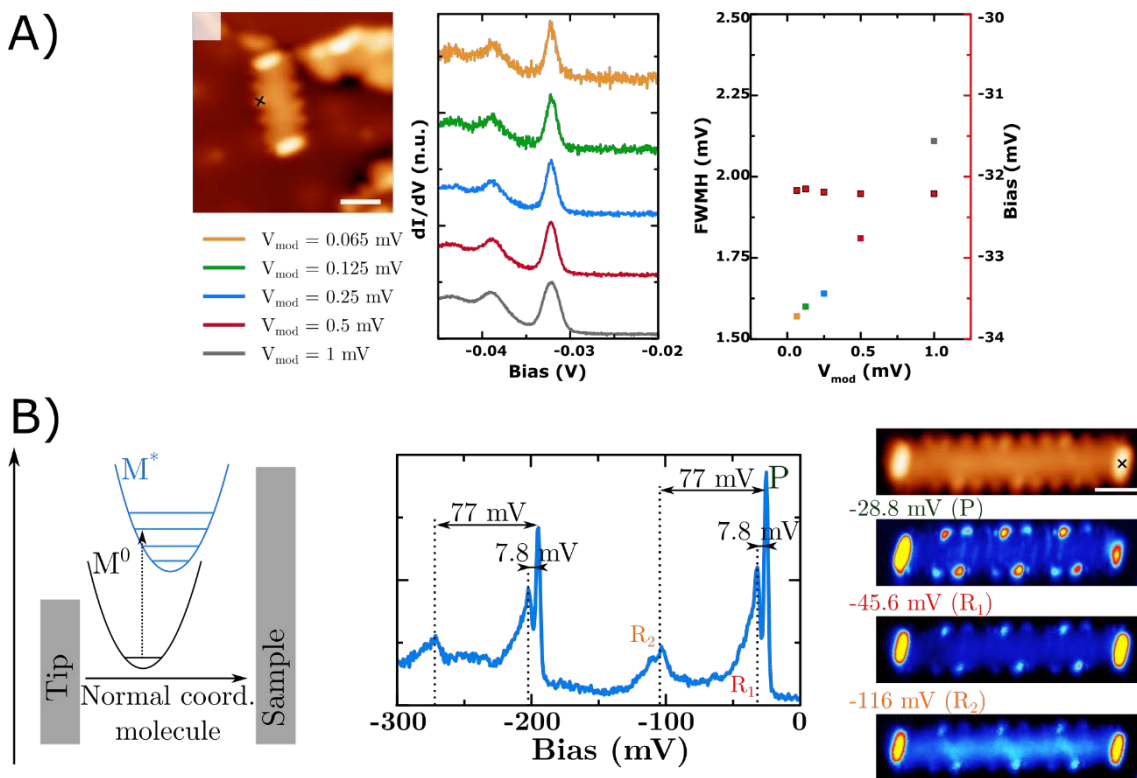


Figure S3. - a) STM topography image of a $L=5$ (3,1,8)-GNRs on MgO_{ML} (0.5 V, 200 pA, $T=1.1$ K, scale bar = 2 nm) and dI/dV point spectra recorded at the position of the cross with varying V_{mod} between 1 and 0.065 mV r.m.s. The left panel shows the experimentally determined FWHM (left axis, colour coded squares) and bias peak values (right axis, red squares) as a function of V_{mod} . b) Sketch of Franck-Condon (FC) mechanism in an STM junction (adapted from ref. [1]) and example of dI/dV spectra with satellite resonances recorded for the (3,1,8)-GNR with $L=11$. The FC resonances are labelled as P, for the main peak, and R_1 and R_2 for the satellite peaks. $V_{\text{mod}}=1$ mV r.m.s. The right panel displays the topography of the GNR (the cross indicates the dI/dV spectroscopy position) and the constant height dI/dV maps recorded at the energies of the main and satellite peaks observed. Notice that all three peaks exhibit identical spatial distribution. Set point for topography, dI/dV stabilization and feedback opening in dI/dV maps is 0.5 V and 200 pA. Lock-in modulation is 1 mV r.m.s. for the dI/dV spectrum and 4 mV r.m.s. for the maps.

Upon insertion of the GNRs onto the MgO, we observe a clear trend of the QW states to shift to lower energies. This is well understood if we look at the variation of the local work function difference ($\delta\Phi_{[\text{Ag-MgO}]}$ in the main text) between the bare Ag(001) and the embedded $\text{MgO}_{\text{ML}}/\text{Ag}(001)$. To characterize this difference we acquired field emission resonances inside and outside of the MgO island shown in Fig. S4a. We observe a marked decrease in the bias difference between consecutive resonances (Fig S4b) in MgO, characteristic of a much lower workfunction. Applying a parallel plate capacitor model for the tip-sample gap [3,4], we can use the higher order resonances to give an accurate estimate of $\delta\Phi=0.7$ eV following the analysis shown in Fig. S4d.

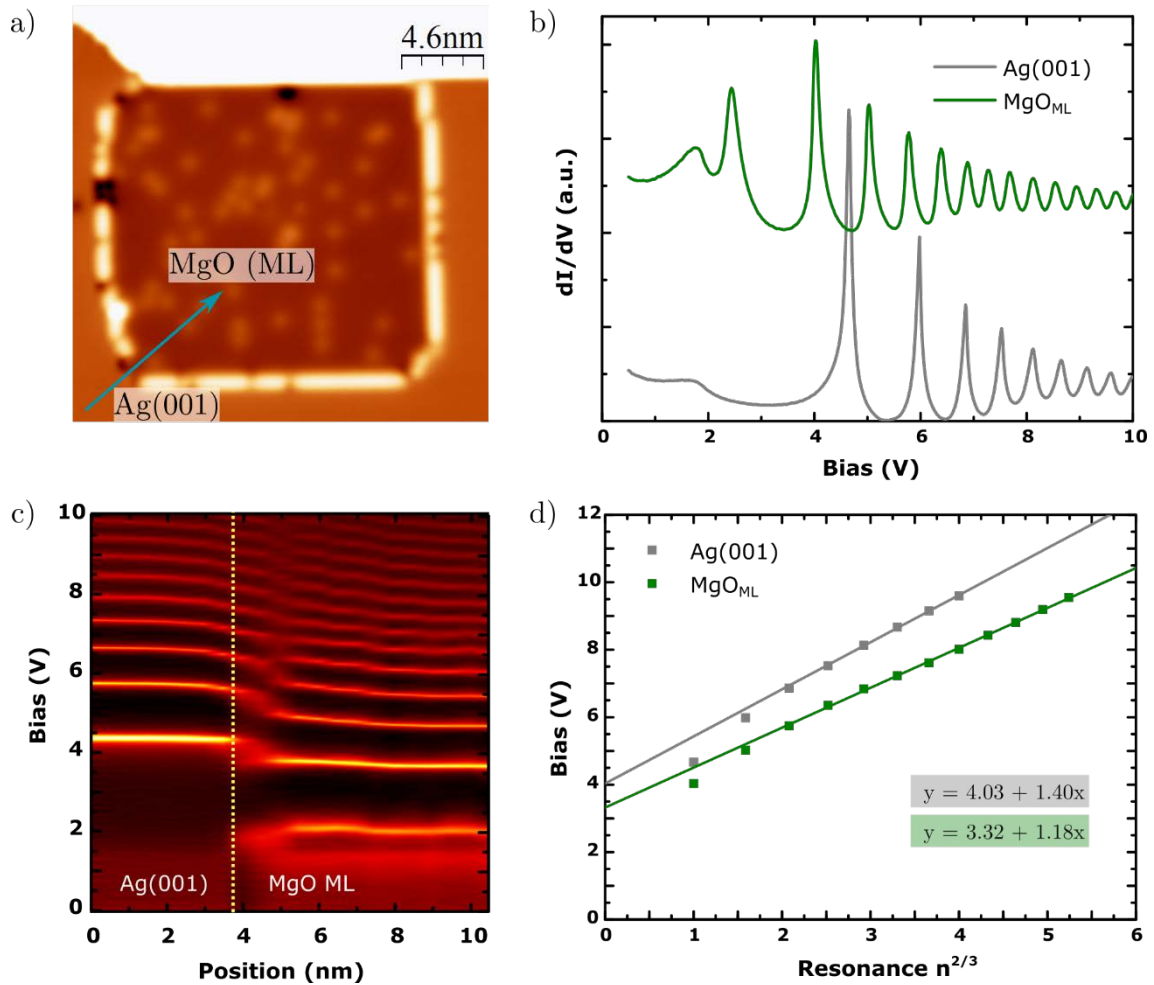


Figure S4. - a) STM image of a MgO_{ML} island embedded in Ag(001). b) Field emission resonance (FER) measurements recorded on Ag(001) and MgO_{ML} island. c) Stack plot of dI/dV spectra recorded along the blue arrow in a). The dotted yellow line corresponds to the Ag-MgO intersection in STM images. d) Peak voltages of FER shown in b) plotted against the resonance order to the power of 2/3. The intersect of the linear fits with the ordinate axis gives a very precise estimate of the work function values (the two first FERs are disregarded because in this regime the 1D approximation for the electric field leading to the model in Refs. [3,4] fails).

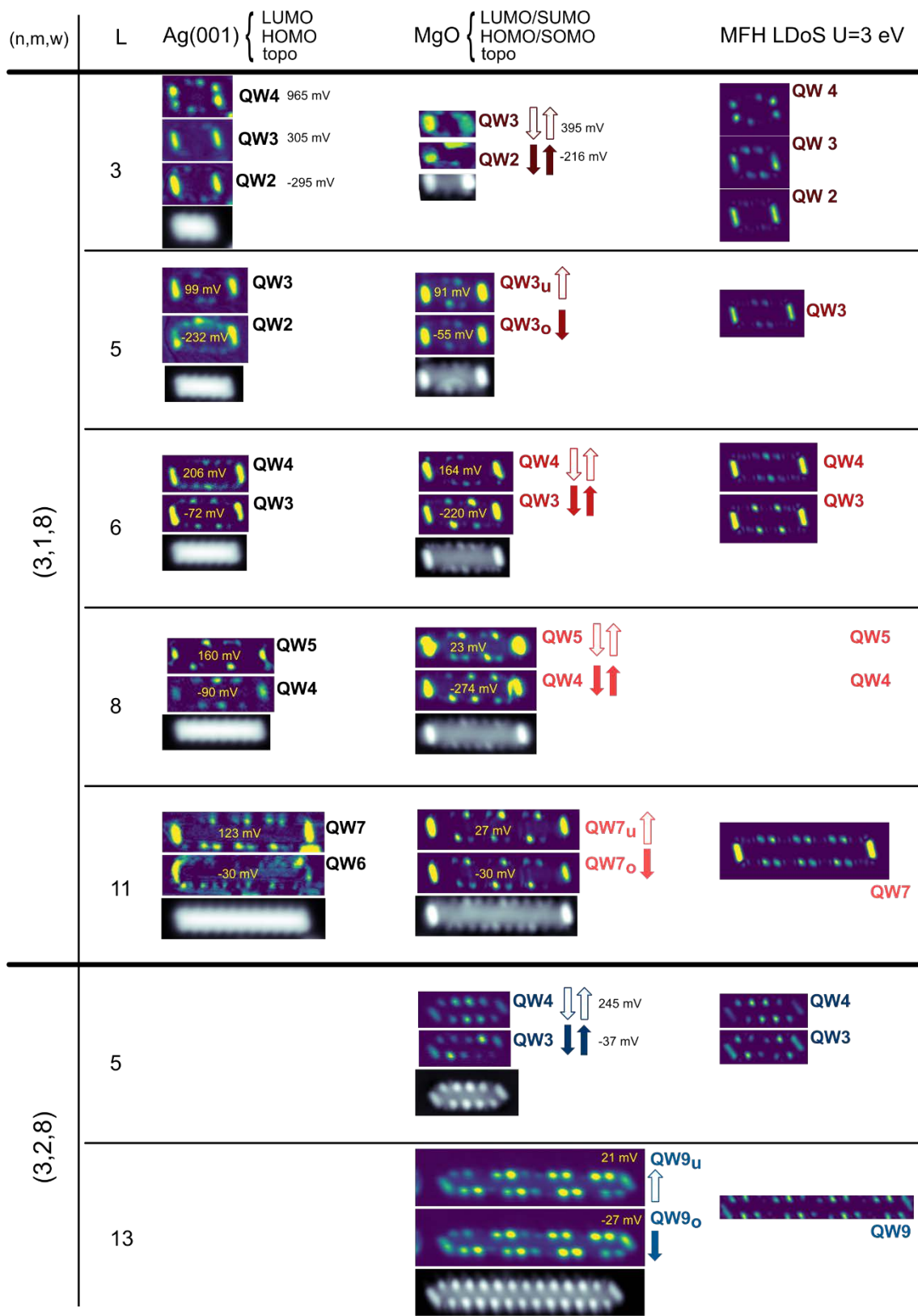


Figure S5.- Collection of experimentally mapped frontier states in Ag(001) and MgO. When the gap in MgO is much smaller than in Ag(001), the two frontier states have the same spatial distribution and thus the ground state becomes spin $\frac{1}{2}$. The comparison with the calculated LDoS QW states with the same spatial distribution allows us to determine the GNRs charge state for each case. STM parameters for GNRs on MgO: constant height scans at the specified sample bias with lock-in modulation of 2 mV rms, except for $L=3$ for which we plot a constant current scan with regulation set point of 500 mV and 20 pA and modulation 4.4 mV rms. STM parameters for GNRs on Ag(001):

constant current maps at the specified sample bias for $L=3, 5, 6, 11$; constant current maps with regulation set point of -300 mV and 100 pA for $L=8$. All topographies (grey scale images) are taken at 500 mV sample bias. Labels and color code of schematic spin states are the same as in Figs. 3 and 4 of the main text.

(n,m,w)	L / pu	Ag(001)			MgO _{ML} /Ag(001)			$\Delta E_{\text{MgO-Ag}}$
		Last occ. QW (k^{th})	INT(#e)	e/PU (\approx)	Last occ. QW (k^{th})	#e	e/PU	Shift ($k+1$) th QW / eV
318	3	2	6	2	2	6	2	+0.075
	5	2	6	1.2	$\frac{1}{2}$ 3	7	1.4	-0.1
	6	3	8	1.33	3	8	1.33	-0.07
	8	4	10	1.25	4	10	1.25	-0.137
	10	4	12	1.2	--	--	--	--
	11	6	14	1.27	$\frac{1}{2}$ 7	15	1.36	-0.123
	12	5	14	1.16	--	--	--	--
328	5				3	8	1.6	
	13	--	--	--	$\frac{1}{2}$ 9	19	1.46	

Table S1.- List of approximate charge states on Ag(001), integer charge states on MgO_{ML} last occupied QW states and shift of the first fully unoccupied QW state. The order of the QW state has been deduced by comparing experimental dI/dV maps of the frontier orbitals with the theoretical LDoS. The $\frac{1}{2}$ symbol indicates that the referred QW state is singly occupied.

Figure S5 collects the experimental LDoS maps of the QW resonances for all the GNRs that were successfully characterized on the MgO_{ML}, together with the corresponding states as they appear on the bare Ag(001). A comparison with the simulated LDoS using the MFH model with $U=3$ eV (see Methods at the main article body), shown in the right hand column, allows us to extract the quantum number associated to the QW order, and thus, the charge state (as explained at the discussion of Fig. 3 of the main text). The so deduced charge states and resulting doping densities for GNRs on Ag and MgO_{ML} are given in Table S1.

The first unoccupied QW state experiences a shift in energy of approximately -100 meV when moving the GNR ($L>3$ PU) from the Ag to the MgO_{ML} (schematically represented by grey dashed lines in Fig. 3 of the main manuscript). Surprisingly, this shift and the concomitant charge transfer from the underlying metal, occurs in a step-wise manner as more PU units are positioned over the MgO during the insertion. This is shown in Fig. S6, where we provide dI/dV spectra of 4 different GNRs in different stages of the lateral atomic manipulation process.

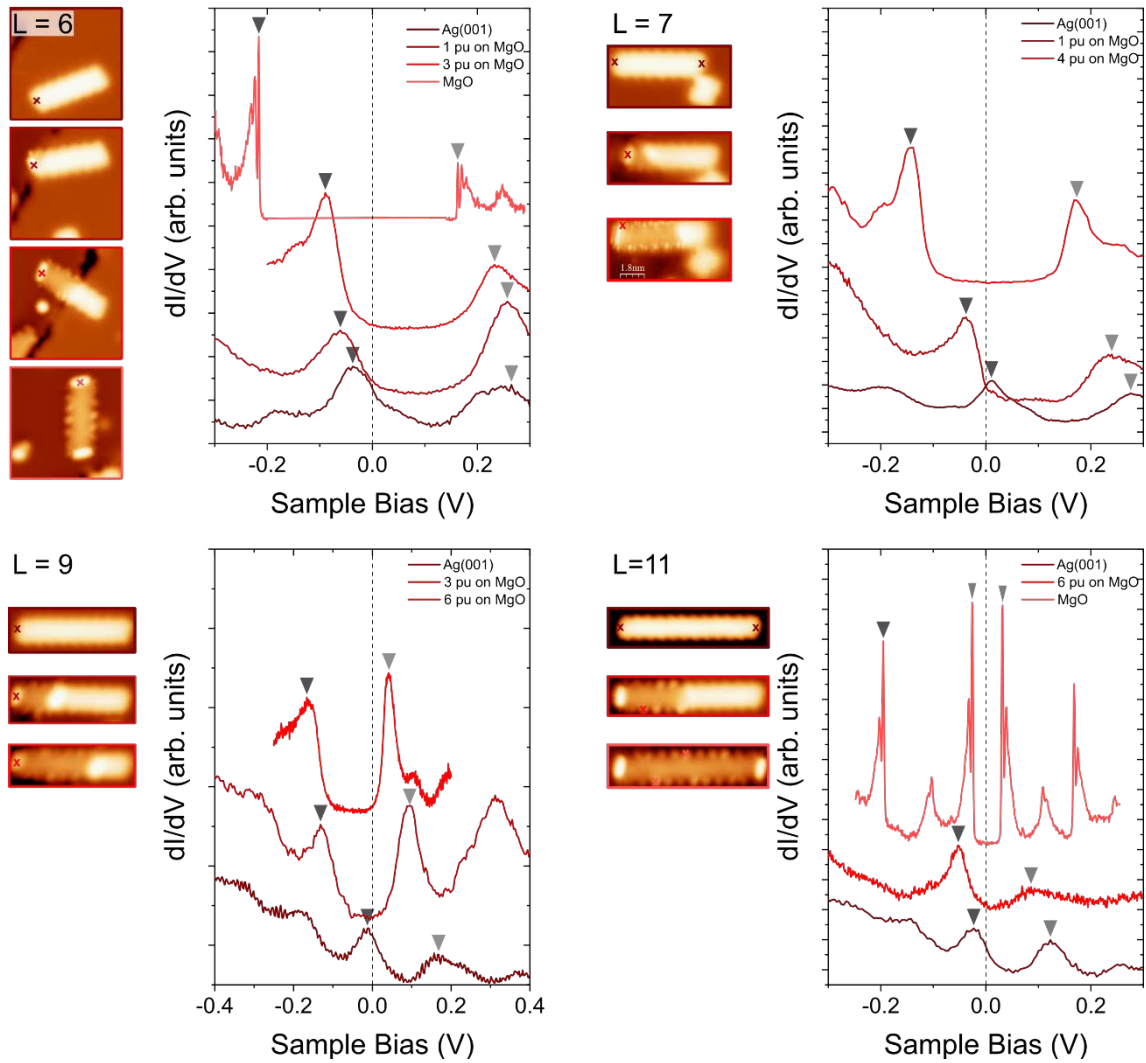


Figure S6.- Gradual insertion of (3,1,8)-GNRs on MgO and concomitant rigid downshift of the QW states. Horizontal image size: $L=6 \rightarrow 8$ nm; $L=7 \rightarrow 9$ nm; $L=9 \rightarrow 9$ nm ; $L=11 \rightarrow 11.5$ nm. The correlations induced splitting of the edge state only appears for fully decoupled ribbons. When some portion of the GNR remains in contact with the Ag(001), the n-doping takes place gradually depending on the length inserted onto MgO_{ML} and metal, but the e-e interaction is partially quenched. This explains why previous attempts with (1,0,6)-GNR/Au(111) partially intercalated with NaCl [5] did not manifest the true discretization observed on our MgO_{ML} patches.

3. Supplementary Theoretical Methods.

It is useful to describe the Ag(100)/MgO_{ML}/GNR system of our experiment as a plate capacitor model formed by components with different electron affinity (E_a). This model is validated in Ref. [6]. The MgO layer acts as electronic decoupler, that hinders the wavefunction overlap between metal and molecular states, and stabilizes integer states in the GNR (rather than fractional, as would happen for direct GNR adsorption on the metal). At the same time, the MgO layer reduces the substrate's work function [7–9]. To reach chemical equilibrium with the metal, the GNR becomes charged by an integer amount of electrons that tunnel from the metal through the MgO layer in response to their difference in electron affinities. The charging of the GNR simultaneously causes an electric field across the MgO that opposes the charging and partially compensates the difference in electron affinities. This component has been described in previous works as an interface dipole that causes deviation from pure vacuum-level alignment [6]. Therefore, in equilibrium these processes are reflected by a shift of the GNR's chemical potential μ with respect to the neutral charge level μ_0 (i.e. by $\Delta\mu = \mu - \mu_0$), which is smaller than the difference in electron affinities owing to the energy U_d stored in the MgO capacitor by the built-up dipole. This is reflected in the following expression

$$\Delta\mu = \mu - \mu_0 = E_a - \Phi - U_d \quad (1)$$

The value of $\Delta\mu$ determines the charge state of a GNR of length L in equilibrium. The two types of chiral GNRs used in the experiment have a non-trivial topological band structure and, therefore, have two symmetry-protected topological (SPT) end states [10]. For the neutral GNR, the two SPT states are half occupied, and therefore the neutral level μ_0 is referenced by their binding energy (Fig. 5a). Upon electron charging, the chemical potential μ will lie either between two LUMO levels of the molecule for even charge (i.e. the closed-shell configuration, singlet spin state) between SOMO and SUMO levels, for the case of odd charge state (open shell, doublet spin state).

To simulate how the GNR charges as a function of length, we describe the system in the grand canonical ensemble and calculate the mean number of excess electrons $\langle q \rangle$ for any given chemical potential μ using the relation

$$\langle q(\mu, L, T) \rangle = -k_B T \frac{dZ(\mu, L, T)}{d\mu} \quad (2)$$

This expression provides a charge value as a function of μ which can be compared with experimental results for every GNR. For a GNR with a given length L and chirality, at the temperature of our experiment (between 1.2 and 4.3 K), we can calculate the grand canonical partition function $Z(\mu, L, T)$ following the expression

$$Z(\mu, L, T) = \sum_j \exp\left(\frac{N_j T - E_j}{k_B T}\right) = \sum_q \exp\left(\frac{j\mu - E_0 - E_q}{k_B T}\right) \quad (3)$$

where N_j is the total number of indistinguishable electrons, and E_j the internal energy of each respective charge state j obtained from MFH simulations (see Methods main text). No overcounting correction is included as we consider each microstate j only once. We note that at cryogenic temperatures, the entropic contribution to the grand potential can be neglected and $\langle q \rangle$ can be obtained equivalently by simply minimizing the right hand side of (3), instead of the total energy. We limit our model to the spin-restricted case, as the mean spin densities on the edge are energetically unstable against the emergence of nodal planes, and thus determining the correct ground state becomes ambiguous for large $(3, n, 8)$ -GNRs doped into the chiral edge band.

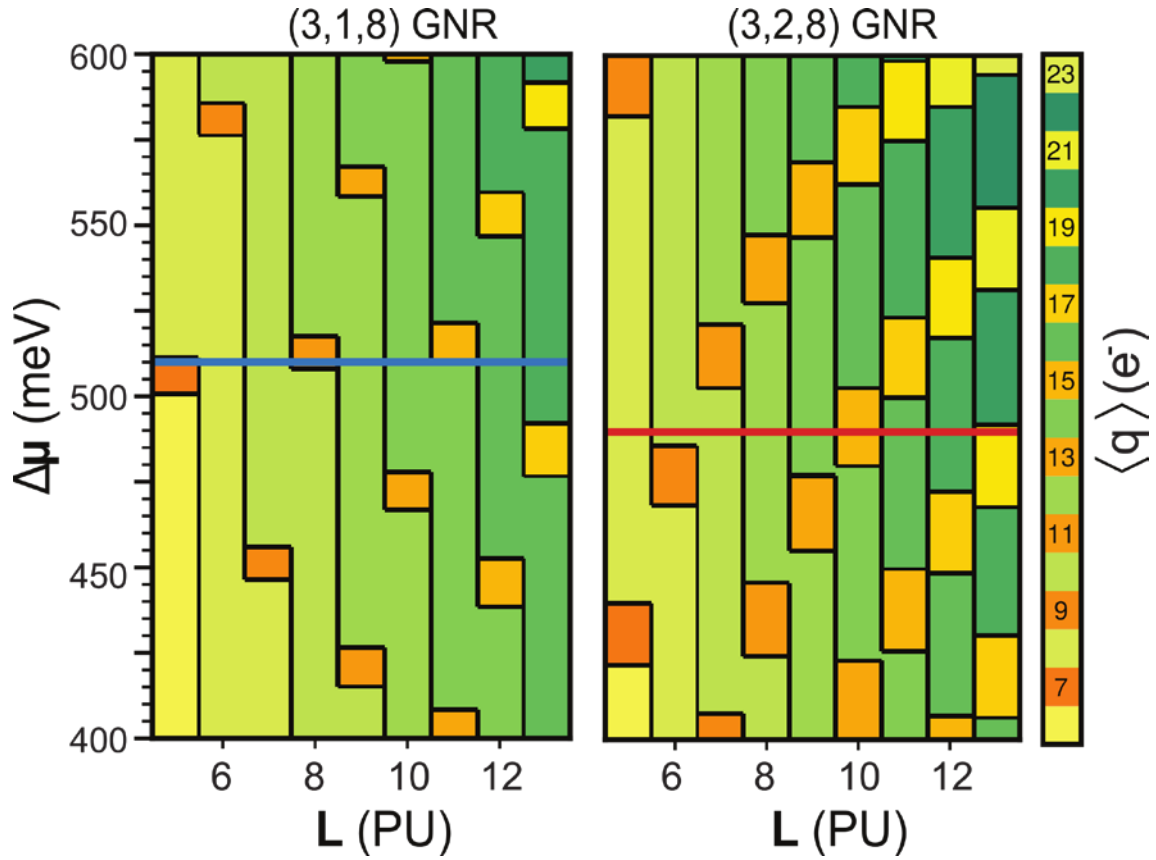


Figure S7: Contour plots of the calculated excess charge for (3,1,8)- (left) and (3,2,8)-chGNRs (right). Even and odd charge states are represented by different color scales. Horizontal lines represent the best-fit values for $\Delta\mu$ to match the experimental charging pattern (see Fig. 5b of the main text).

Figure S7 maps the predicted charge patterns as a function of GNR's length as the chemical potential shifts $\Delta\mu$ from 400 to 600 meV. The map reflects the increase in charge with length for both chiralities, and the peculiar odd-even (orange-green) charge pattern that depends on the value of $\Delta\mu$. Comparing the charging patterns with the experimental charge states of the GNRs (Fig. 4 of the main text), an estimated value for $\Delta\mu$, the chemical potential shift, is determined and represented in Fig. S7 by horizontal lines. The theoretical pattern and its comparison with experiments is plotted in Fig. 5b of the main text. The only deviation occurs for the ribbon (3,1,8)-GNR with $L=8$, which appears with even electron occupation ($q=10$) in the experiment, while in the map is expected to have 11 elementary charges. As discussed in the following, small variation of $\Delta\mu$ caused by local defects in the MgO layer can explain this discrepancy.

4. Electrostatic gating of chiral graphene nanoribbons on MgO.

As shown in Fig. S8a-c and Fig. 2 of the main article, when the tip moves laterally across the GNRs on MgO we often observe a rigid shift of all energy levels, ΔE_p (which would not be visible in the case of molecular orbitals spanning in an energy range wider than the maximum $\Delta E_p \sim 20$ meV). In several cases we have been able to find a direct relationship between the ΔE_p and the lateral tip distance to point defects of the MgO that can be detected either below the GNR or next to it. In Fig. S8 we present an example of this effect for the (3,1,8)-GNR with $L=11$ discussed in the main text.

If we apply the Feature Detection STS method [11] to compose a map of the area enclosed by a spectroscopic feature with the shape of the QW resonances (i.e., a peak with FWHM of 1.5 mV, see Fig. S3), the intensity pattern of the QW edges is evenly distributed at the locations predicted by MFH simulations (Fig. S8d). This is in contrast with the case of constant height dI/dV maps at a given energy of the same GNRs, where some lobes of the QW state appear brighter than others (see for example Fig. S5 or Fig. 3b). The reason is that as the tip position $\vec{r} = (x, y, z)$ departs from the defect at $\vec{r}_0 = (x_0, y_0, z_0)$, the electrostatic potential energy at the defect $U_e(\vec{r} - \vec{r}_0)$ varies. Indeed, it has been previously shown that the electric field in the tip-sample gap can modify controllably the electric polarization of thin insulating layers [12], specially next to point defects and vacancies. This gives rise to a variation of the local value of $\Delta\mu(\vec{r} - \vec{r}_0)$ which, in the parallel plane approximation, will be proportional to U_e . This effect can be viewed as an effective gating of the molecular states of the GNRs.

The location of the defect can be pulled out from measurements of the tip induced charging resonances of the defect states [13,14]. They manifest as sharp ellipsoidal rings in the (x, y) plane enclosing the region for which $U_e(\vec{r} - \vec{r}_0)$ is large enough as to charge (positively or negatively) the defect at a constant $z - z_0$. Fixing V_b at a large value of 0.5 V, the size of the charging ring must depend linearly on the tip sample distance, or equivalently, logarithmically on the current set point I_t before opening the feedback (see Figs. S8e-k). As shown in Fig. S8j, we can determine accurately the defect position as the centre of an ellipse fitting the charging ring for different tip heights.

Alternatively, the defects can be found in atomically resolved images of the MgO patch after removing the GNR under study, as illustrated in Fig. S9. Here, we show how the QW states of the (3,1,8)-cGNR with $L=5$ PU can be shifted in energy by changing the distance to a point defect on MgO_{ML}. The GNR in position γ lies over a defect free region of the MgO, and displays a correlation gap between singly occupied frontier states –as predicted by the model discussed in supplementary theoretical methods-. In contrast, when the GNR lies over a point defect (position α) or next to the MgO bilayer edge (position β), the 3rd QW state (see Fig. S5) is shifted in energy above the Fermi level and becomes fully unoccupied, yielding another charge ($q=6$ electrons instead of 7) and total spin ($S=0$ instead of $S=1/2$).

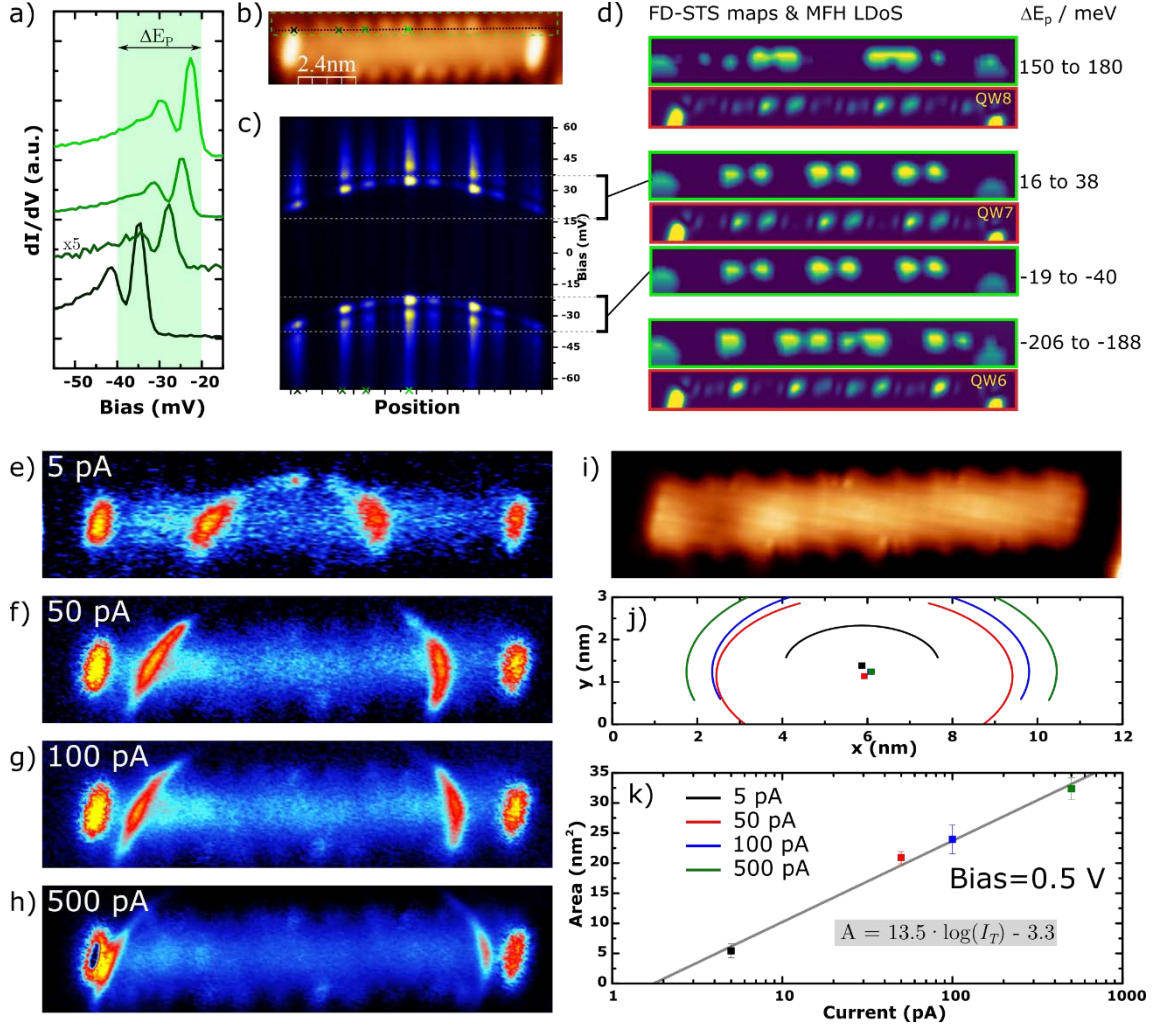


Figure S8.- Gating energy levels by lateral tip positioning. a-c): Shift in energy along the chiral edge of the (3,1,8)-GNR with $L=11$. (STS set point: 0.5 V, 200 pA, $V_{\text{mod}}=1$ mV). a) STS spectra recorded at different positions of the chiral edge. b) STM topography image of the $L = 11$ (3,1,8)-GNR including crosses where STS spectra shown in (a) are recorded. Image set point: 0.5 V, 100 pA. c) Stack plot of dI/dV versus position recorded on the chiral edge of the GNR shown in b) (dotted line). d) Feature-Detection STS [11] intensity maps tuned to a peak with linewidth ≤ 2 mV in the energy range ΔE_p indicated on the right column. Due to the high spatial and energy resolution required for this analysis, we only studied the frame enclosed by the dashed green rectangle in (b). Each experimental map is compared with the corresponding theoretical LDoS of the QW states obtained from the MFH model with $U=3$ eV and $q=15$ electrons (see theoretical methods at the main text) for the $L = 11$ (3,1,8)-GNR. e-k) Determination of the location of point defects in MgO_{ML} by high bias mapping. e-h) Series of constant height dI/dV maps recorded at 0.5 V with tunnelling current set points from 5 to 500 pA at the time of feedback opening over the ribbon centre ($V_{\text{mod}} = 4$ mV). i) In-gap constant height STM image of the GNR shown in e-h) ($V_b=-2.5$ mV). j) Fits (lines) and centers (squares) of the ellipses extracted from the dI/dV maps. k) Area of the ellipses as a function of set point tunnelling current.

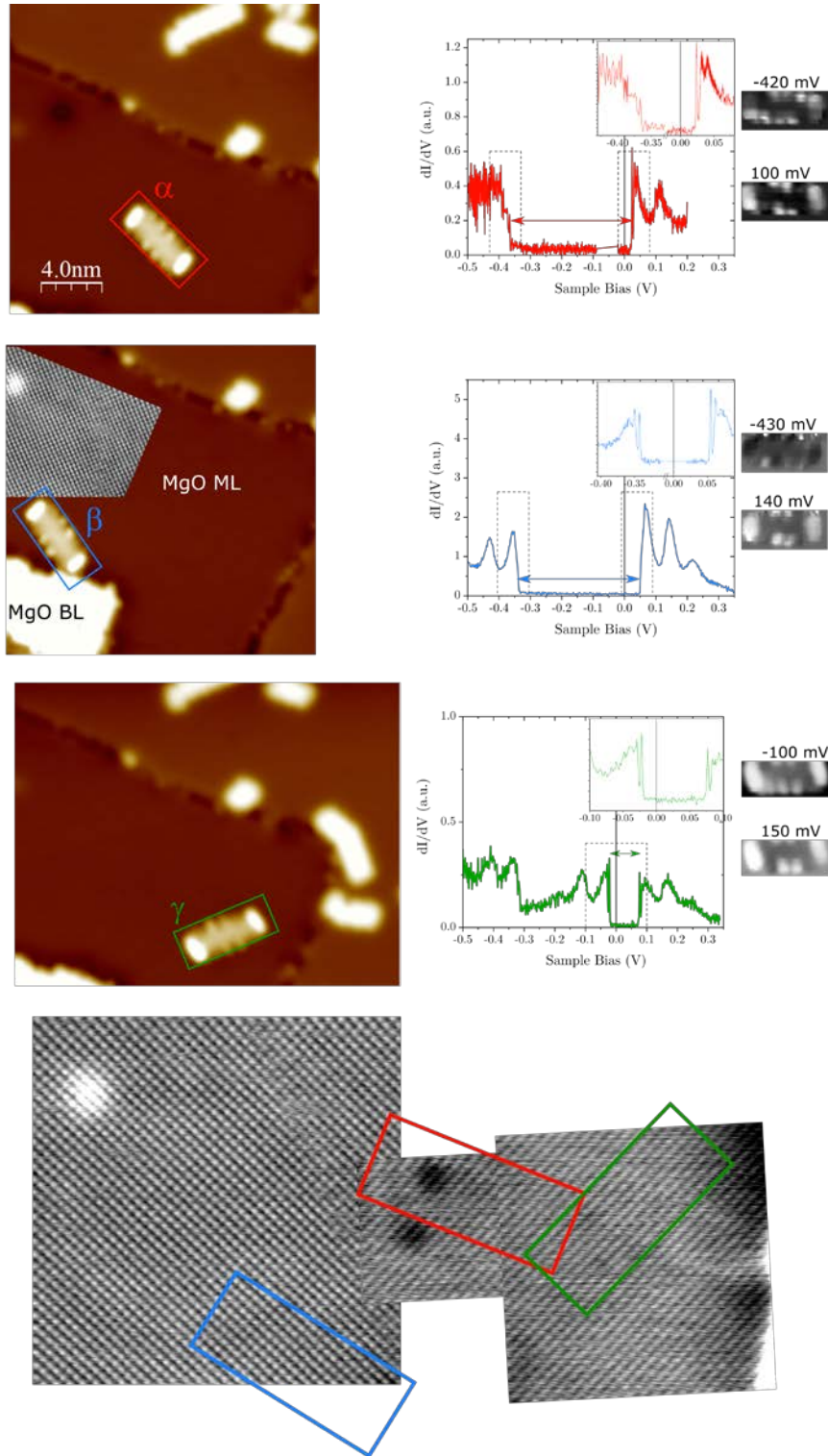


Figure S9.- Gating electron occupancy by GNR position. Data corresponds to the $L=5$ (3,1,8)-GNR. $V_{\text{mod}}=1$ mV and 0.5 mV r.m.s. for spectra in main panels and in the insets, respectively (except for the β position, for which the main panel spectra is taken with $V_{\text{mod}}=5$ mV). The maps of the QW states are tunnelling current images taken at the referred energies but regulating at each pixel at 0.5 V. The three upper panels show the same GNR at three different positions over the MgO patch. As shown in the atomically resolved image of the substrate (grey color scale), in position α the GNR is over a dark spot and next to the bright defect on MgO. It features a normal quantization gap and $q=6$ electrons and therefore total spin $S=0$. Position β is next to the MgO bilayer (BL) island, and the GNR has same charge/spin state as in α . However, at the γ position, farther away from all types of defects, the GNR

is over a defect free region of the MgO, and now exhibits a much smaller gap, as corresponds to the correlations gap. In this latter case, the current map integrating the resonance of the frontier states are the same at both sides of the Fermi level, and thus it has $q=7$ electrons (odd occupancy) and total spin $S=1/2$.

5. Supplementary References

- [1] G. Reece, N. Krane, C. Lotze, L. Zhang, A. L. Briseno, and K. J. Franke, *Vibrational Excitation Mechanism in Tunneling Spectroscopy beyond the Franck-Condon Model*, Phys. Rev. Lett. **124**, 116804 (2020).
- [2] J. van der Lit, M. P. Boneschanscher, D. Vanmaekelbergh, M. Ijäs, A. Uppstu, M. Ervasti, A. Harju, P. Liljeroth, and I. Swart, *Suppression of Electron-Vibron Coupling in Graphene Nanoribbons Contacted via a Single Atom*, Nat Commun **4**, 2023 (2013).
- [3] J. Bono and R. H. Good, *Conductance Oscillations in Scanning Tunneling Microscopy as a Probe of the Surface Potential*, Surface Science **188**, 153 (1987).
- [4] O. Yu. Kolesnychenko, Yu. A. Kolesnichenko, O. I. Shklyarevskii, and H. van Kempen, *Field-Emission Resonance Measurements with Mechanically Controlled Break Junctions*, Physica B: Condensed Matter **291**, 246 (2000).
- [5] S. Wang, L. Talirz, C. A. Pignedoli, X. Feng, K. Müllen, R. Fasel, and P. Ruffieux, *Giant Edge State Splitting at Atomically Precise Graphene Zigzag Edges*, Nature Communications **7**, 11507 (2016).
- [6] P. Hurdax, M. Hollerer, P. Puschnig, D. Lüftner, L. Egger, M. G. Ramsey, and M. Sterrer, *Controlling the Charge Transfer across Thin Dielectric Interlayers*, Adv. Mater. Inter. **7**, 2000592 (2020).
- [7] M. Hollerer, D. Lüftner, P. Hurdax, T. Ules, S. Soubatch, F. S. Tautz, G. Koller, P. Puschnig, M. Sterrer, and M. G. Ramsey, *Charge Transfer and Orbital Level Alignment at Inorganic/Organic Interfaces: The Role of Dielectric Interlayers*, ACS Nano **11**, 6252 (2017).
- [8] G. Witte, S. Lukas, P. S. Bagus, and C. Wöll, *Vacuum Level Alignment at Organic/Metal Junctions: "Cushion" Effect and the Interface Dipole*, Appl. Phys. Lett. **87**, 263502 (2005).
- [9] H.-J. Freund and G. Pacchioni, *Oxide Ultra-Thin Films on Metals: New Materials for the Design of Supported Metal Catalysts*, Chem. Soc. Rev. **37**, 2224 (2008).
- [10] J. Li, S. Sanz, N. Merino-Díez, M. Vilas-Varela, A. Garcia-Lekue, M. Corso, D. G. de Oteyza, T. Frederiksen, D. Peña, and J. I. Pascual, *Topological Phase Transition in Chiral Graphene Nanoribbons: From Edge Bands to End States*, Nat Commun **12**, 5538 (2021).
- [11] J. Martinez-Castro et al., *Disentangling the Electronic Structure of an Adsorbed Graphene Nanoring by Scanning Tunneling Microscopy*, Commun Mater **3**, 57 (2022).
- [12] J. Martinez-Castro, M. Piantek, S. Schubert, M. Persson, D. Serrate, and C. F. Hirjibehedin, *Electric Polarization Switching in an Atomically Thin Binary Rock Salt Structure*, Nature Nanotechnology **13**, 19 (2018).
- [13] C.-L. Song, Y.-P. Jiang, Y.-L. Wang, Z. Li, L. Wang, K. He, X. Chen, X.-C. Ma, and Q.-K. Xue, *Gating the Charge State of Single Fe Dopants in the Topological Insulator Bi_2Se_3 with a Scanning Tunneling Microscope*, Physical Review B **86**, (2012).
- [14] M. S. G. Mohammed, L. Colazzo, R. Robles, R. Dorel, A. M. Echavarren, N. Lorente, and D. G. de Oteyza, *Electronic Decoupling of Polyacenes from the Underlying Metal Substrate by Sp^3 Carbon Atoms*, Commun Phys **3**, 159 (2020).